UC Berkeley
UC Berkeley Previously Published Works

Title
Pyroclast cooling and saturation in water

Permalink
https://escholarship.org/uc/item/1579n1bj

Authors
Fauria, Kristen E
Manga, Michael

Publication Date
2018-08-01

DOI
10.1016/j.jvolgeores.2018.07.002

Peer reviewed

Pyroclast cooling and saturation in water

Kristen E. Fauria[ab] Michael Manga[a]

Abstract

In the submarine setting pyroclast cooling and saturation, by controlling the buoyancy of individual clasts and surrounding fluid, exert fundamental controls on the dispersal and fate of volcanic material. In this study we use laboratory experiments to understand and quantify how hot and air-filled pyroclasts cool and saturate in liquid water. By measuring internal temperature and clast submerged weight in over thirty experiments, we find that pumicecools and saturates in two stages. We observe that the first stage is marked by much higher rates of cooling and saturation than the second stage and that the transition between stages is sharp. We propose conceptual and quantitative models for each stage of pyroclast cooling and saturation. Specifically we argue that the first stage is defined by the presence of internal steam. That is, hot pyroclasts ingest liquid water and generate steam. Once a clast's internal pore space is filled with steam, heat loss to the surroundings causes condensation of internal vapor and clast saturation. Stage 1 ends when all internal steam has condensed. We test this idea with a Stefan Model with advection and conclude that heat loss, rather than permeability, controls the saturation of pyroclasts above the boiling temperature. We find that permeability matters for air-filled clasts with initial temperatures below the boiling point. Stage 2 begins after all internal vapor has condensed and we propose that stage 2 cooling and saturation are controlled by heat conduction and thermal contraction of trapped gas, respectively. From our understanding of the processes that govern the stage 1 to 2 transition, we derive an empirical average pyroclast cooling rate of $q = 7.5 \pm 0.5$ W cm^{-2}. Finally, we develop quantitative models for cooling-controlled porous clast saturation and for buoyant clast rise to the ocean surface. We find that meter size clasts stay buoyant for more than 10 min - long enough to reach the surface from a depth of 1000 m. The models developed here test our understanding of clast-scale processes and demonstrate that - in hot and porous clasts - the details of internal texture do not matter because clast saturation, and thus buoyancy and fate in the water column, are governed by heat transfer.

1. Introduction

When pyroclasts erupt into or onto water they are known to at least partially saturate and cool. Experiments show that the water logging of hot lapilli-size pyroclasts can be rapid (e.g., Whitham and Sparks, 1986, Allen et al., 2008, Jutzeler et al., 2017 and pyroclast cooling is thought to provide buoyancy for submarine plumes (e.g., Head and Wilson, 2003, White et al., 2015. In this study we experimentally measure pumice cooling and saturation rates in

liquid water and develop models for clast-scale cooling and saturation behaviors. Because cooling and saturation control buoyancy, a clast-scale understanding is central for testing and building models of submarine plumes and pyroclast dispersal.

In the subaerial environment, the fate of pyroclastic material depends on heat transfer, where heat loss from pyroclasts makes plumes buoyant and can control the runout of pyroclastic density currents. Clast-scale models for heat transfer (e.g., Thomas and Sparks, 1992, Stroberg et al., 2010 have therefore become foundational for multiphase models of subaerial volcanic flows (e.g., Ongaro et al., 2007, Dufek and Bergantz, 2007, Benage et al., 2016. Clast-scale models for heat transfer in water are likewise necessary to understand and build quantitative models for submarine eruption dynamics. We expect, however, that pyroclast cooling in water may be complex because water is an effective coolant, porous pyroclasts can ingest water, and phase changes are possible.

In the subaqueous setting, pyroclasts can also themselves be buoyant. It is known that submarine eruptions can generate rafts of floating pumice (e.g., Bryan et al., 2004, Jutzeler et al., 2014, Carey et al., 2014b. Pumice can stay afloat for months to decades (e.g., DeVantier et al., 1992) due to gas trapping and can sink because of gas diffusion (Fauria et al., 2017) or may wash ashore.

Experiments have demonstrated that hot (> 300°C) pumice can sink rapidly, often within several seconds, and that the tendency for pyroclasts to saturate increases with clasttemperature (Allen et al., 2008, Jutzeler et al., 2017, Whitham and Sparks, 1986). Whitham and Sparks (1986) suggested that hot pyroclasts generate steam in their pore spaces as they ingest liquid water and that steam generation drives air out. Allen et al. (2008) further argued that the condensation and contraction of steam drives pyroclast saturation and that "pumice lapilli cool and adsorb water more readily than larger clasts." These findings suggest that there is a direct connection between pyroclast cooling and saturation.

Conceptual models for submarine plumes often incorporate these observations that pumice can be both positively and negatively buoyant and that heat loss plays a role in dictating buoyancy. For example, Kano et al. (1996) envisions a submarine plume containing both rising and falling clasts and where "hot pumice clasts, especially large ones ... ascend in plume by buoyancy... [while] clasts of smaller sizes rapidly cool down in contact with water and begin to fall out from the plume." Similarly, Allen and McPhie (2009) depict submarine eruptions where giant pumice can remain hot and buoyant long enough to reach the surface and Cashman and Fiske (1991) model how pumice size and density dictate clast fallout behavior. The idea that pyroclasts from a single eruption can be sorted into floating and sinking components based, at least in part, on saturation and heat transfer dynamics is consistent with the recent observation that most, but not all, pyroclasts

from the 2012 eruption of Havre submarine caldera formed a raft and that larger clasts were dispersed farther (Carey et al., 2018). Work remains, however, to quantitatively test these and other conceptual models for submarine eruption dynamics and pumice transport.

In this study we first use laboratory experiments to examine clast-scale cooling and saturation in water. We then propose that different processes control cooling and saturation dynamics at different stages in time (Section 3.3). In Section 4 we develop quantitative models to test our conceptual models for the stages of pyroclast cooling and saturation.

We conclude, based on agreement between experimental and model results, that hot pyroclasts cool and saturate in two main stages. In the first stage, hot clasts convert ingested water to steam. Clast cooling then causes the condensation of internal water vapor and drives saturation. In the second stage, we conclude that clasts cool by conduction and saturate due to the the thermal contraction of trapped non-condensable gases.

We use the models validated in Section 4 to expand beyond our experimental parameter range and examine behaviors relevant for submarine pyroclast-producing eruptions (Section 5). Specifically, we use our models to determine if (and how quickly) steam-filled clasts exiting a submarine vent (1000 mbsl) can reach the ocean surface (Section 5.2). Together, our experimental and model results demonstrate how cooling limits water ingestion and why hot clasts often reach the ocean surface. The clast-scale models developed here can be used in multiphase and multicomponent models for submarine clast-producing eruptions and our experiments can be used to validate future models that incorporate additional physics such as pressure effects.

2. Experimental methods

We conduct laboratory experiments to examine how air-filled pumice cool and saturate in water primarily using clasts from Medicine Lake, California and also from the 1902 plinian eruption of Santa Maria Volcano, Guatemala and rafted pumice from the 2012 eruption of Havre submarine volcano, Kermadec Arc (Table 1). The Medicine Lake clasts originated from the Plinian fallout phase before the 1060 CE emplacement of the Glass Mountain flow. Porosities of 0.69–0.81 with connected fractions of 0.81–0.97 have been measured on Medicine Lake clasts (Giachetti et al., 2015). We use subaerial clasts because they are similar in vesicularity and macrotexture to their submarine counterparts (e.g., Rotella et al., 2015) and more readily available. While the signatures of magma-water interactions on pyroclast textures can be difficult to recognize (e.g., White et al., 2015) and subaerial and submarine clasts have overlapping vesicularities and permeabilities (e.g., Carey et al., 2014a), open questions exist about the differences in internal structure of submarine versus subaerial pumice that can be addressed with future micro-textural studies.

Table 1. Pumice clast characteristics: characteristic radius, r_o, is estimated by assuming a spherical geometry and * refers to values calculated by assuming porosities (70% for Pum08 and 80% for HRaft01). n refers to the number of experiments conducted on each clast. rtro refers to the thermocouple position relative to clast radius, rtro=1 implies that the thermocouple is at the center of the clast. Uncertainties are calculated as the standard deviation of a set of measurements. We do not report uncertainties where only one measurement was made or if multiple measurements report the same values.

Clast name	Source	Mass (g)	Volume (cm³)	Porosity	r_o(cm)	rtro	n	Bi	HWm2K
ML01	Medicine Lake, CA	7.7	11.1	0.70	1.4	0.73	9	3.6±0.6	194±35
ML02	Medicine Lake, CA	38.9	50.5	0.67	2.3	0.65	9	9.9±3.6	314±115
ML03	Medicine Lake, CA	7.9	11.6	0.70	1.4	0.71 &0.35	4	4.3±0.5	223±29
Pum06	unknown	5.7	6.8	0.64	1.2	0.68	2	5.5±0.5	359±33
SM16	Santa Maria, Guatemala	4.3	7.0	0.74	1.2	0.67	1	4	240
Pum07	Medicine Lake, CA	63.8	83.2	0.67	2.7	0.70	2	6	167
Pum08	Medicine Lake, CA	302.2	*403.0	*0.70	*4.6	*0.87	1	2	33
HRaft01	Havre 2012 raft	60.7	*121.4	*0.80	*3.0	*0.98	1	1	20

In the experiments presented here, we measure pumice submerged weight through time to calculate and quantify liquid saturation. At the same time, and to examine cooling, we measure pumice internal temperature at one or two locations within the clasts. We explore a parameter range that includes 2 to 9 cm diameter pumice and initial temperatures from ambient to 670°C (Tables 1 and S1).

To measure pumice internal temperature, we place K-type thermocouples (temperature range up to 1335°C) into 2 mm diameter drilled holes within the clasts. While we attempted to center the thermocouple within the clast, irregular clast shapes made centering the thermocouple imprecise and not well defined. Table 1 gives rtro, the ratio of thermocouple location to clast spherical equivalent diameter, for each clast. We use Al cement to secure and seal the space between the clast and thermocouple.

We heat clasts in one of two different ovens with the thermocouple/s adhered and the thermocouple sheathing bent to fit through gaps in the oven doors. Because one of our ovens has a temperature range less than 260°C and the other oven has a temperature range greater than 460°C, we do not conduct experiments within the 260–460°C range.

To initiate an experiment, we remove the clast from the oven and quickly submerge the clast 1 to 3 cm below the surface of a 20°C water bath (Fig. 1). The water bath is large (twelve liters), as is the heat capacity of water, such that we expect temperature gradients within the bath to be minimal. Indeed, we do not observe changes in background temperature as the clasts cool.
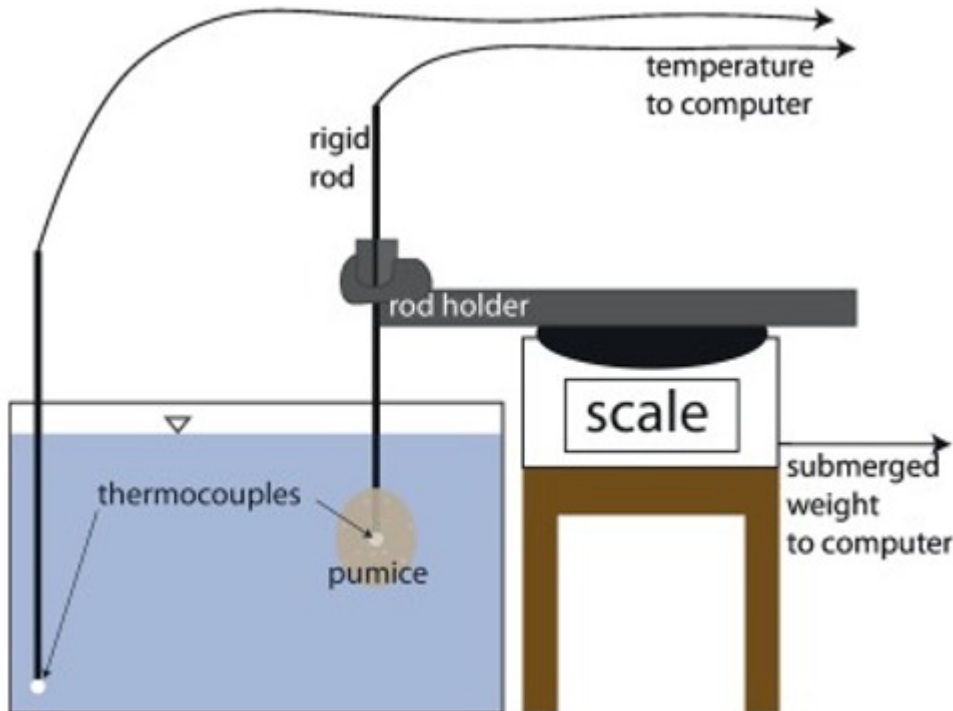

Fig. 1. Experimental set-up. We measure the internal temperature and submerged weight of pumiceclasts as they cool in a water bath.

As the clast is submerged, we record clast internal temperature and water bath temperature at 0.42 Hz. When two thermocouples are present in a clast, we can observe temperature gradients in a single clast. We do not assume that temperature is uniform within a clast.

We measure clast submerged weight at 1 Hz by connecting a rigid rod extending from the thermocouple(s) to the scale (Fig. 1). Because the pumice enter the water before the rigid rod is placed on the scale, there is a 1–2 second delay between the time the clast is submerged and the time when we begin measuring submerged weight. Submerged weight increases as a pumice becomes saturated because the downward force exerted on the scale is proportional to pumice density, which increases as a clast saturates. Clasts are often initially buoyant, however the rigid rod keeps the clasts below the water surface. Buoyant clasts push up against the rigid rod such that their buoyancy is reflected in the submerged weight measurement.

Pumice submerged weight is the clast out-of-water weight, M_T, less the displaced water weight,

$$(1) \quad M_S = M_T - \rho_l V_T,$$

where V_T is the pumice volume, and ρ_l is liquid water density. We determine pumice volume, V_T, by separately measuring the submerged weight of a dry clast and where we sealed the clasts with wax paper (parafilm) (Houghton and Wilson, 1989). Porosity is estimated from clast dry weight and volume (Table 1). We do not measure porosity on two large clasts that were too big for our ballast. We directly measure M_S during the experiments.

We relate the change in submerged weight, M_S, to the change in volume of liquid water within the pore space of a clast, V_l, according to

$$(2) \quad \Delta MS = \rho l \Delta Vl,$$

where ρ_l is liquid water density. We calculate the flux of liquid water, Q_l into the pumice according to

$$(3) \quad Ql = dMSdt,$$

where t is time, and Q_l has units of grams per second. We report Q_l and ΔM_S rather than $M_S$because the weight of the thermocouple wire added uncertainty ($\pm$ 3 g) to M_S but did not affect the accuracy of ΔM_S.

3. Experimental results

We first describe observations of cooling and saturation of a single and representative pyroclast. We then describe how cooling and saturation depend on clast initial temperature. Finally, we identify several general sets of behavior that occur as pumice cool in liquid water and suggest what processes control cooling and saturation behaviors.

3.1. Cooling and saturation of a representative clast

Here we describe the cooling and saturation of a representative 7.9 g clast from Medicine Lake, California (ML03) from an initial temperature of 265°C (Fig. 2). We placed thermocouples at two locations within ML03, 6 and 11 mm from the edge, and report change in submerged weight as $\Delta M_S = M_S(t) - M_S(t = 0)$.
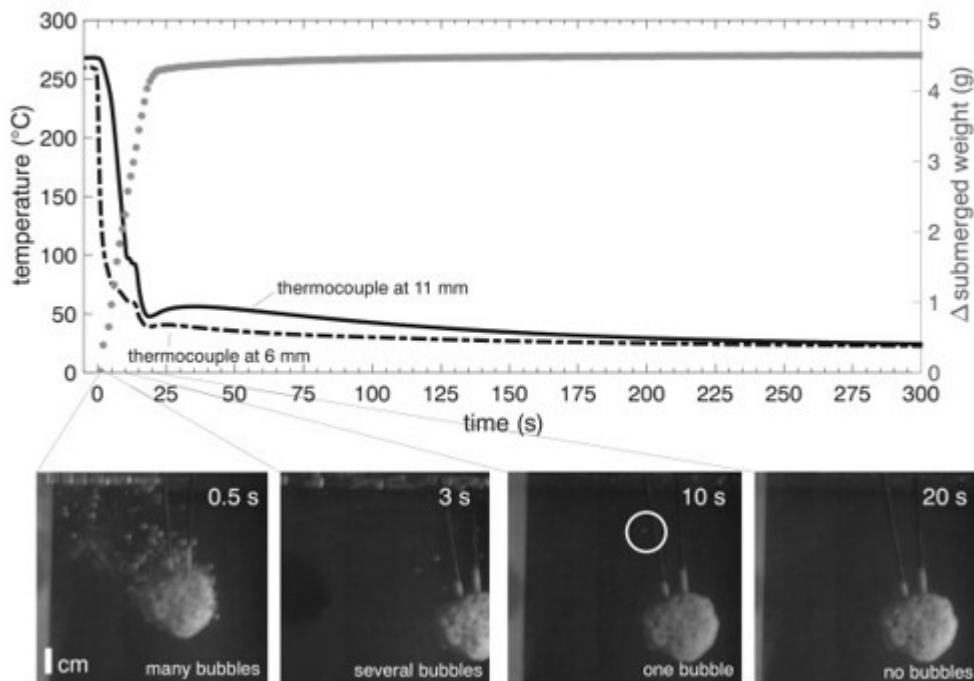
Fig. 2. Cooling and saturation of 7.9 g Medicine Lake clast ML03 from an initial temperature of 265°C. We measure internal temperature at two locations within the clast: 6 and 11 mm from the clast edge (solid lines). We find that submerged weight increases and internal temperatures drop rapidly in the first 19 s following submersion (dotted line). We observe bubbles flowing in the first 3–5 s following submersion. We find that ΔM_S decreases at the same time (~19 s) internal temperatures reach local minima.

We find that the submerged weight of ML03 increases immediately following submersion and gas bubbles (air) vigorously flow out (Fig. 2). Internal clast temperature drops more than 150°C within the first 10 s following submersion.

The rate of visible gas bubble escape slows within the first several seconds following submersion, yet clast submerged weight continues to increase. At 10 s, the temperature recorded by the 11 mm thermocouple approaches 100°C before falling rapidly.

At 19 s, we observe an inflection point in submerged weight, indicating a decline in liquid flux into the clast. At ≈ 19 s, we also observe local minima in temperature at both thermocouples, after-which temperature increases at both thermocouples before declining again.

Experiments on other clasts and at other initial temperatures exhibit similar behavior. Specifically, we find that clasts with initial temperatures greater than the boiling point (100°C at 1 atm) exhibit a sharp transition between high initial liquid flux stage and second low liquid flux stage (Fig. 2).

At the time of this high-to-low liquid flux transition, we observe corresponding changes in temperature. In some clasts (e.g., Fig. 2) we observe local minima in the temperature and in others we see an inflection

point (e.g., Fig. S1). Regardless of the specificities of observed temperature time series, we find that internal clast temperature is always ≤ 100°C at the high-to-low liquid flux transition. We emphasize that all our experiments were done at 1 atm.

3.2. Initial temperature effects

To determine how clast initial temperature and thermal energy affect cooling and saturation, we conducted experiments where we varied the initial temperatures of two clasts from Medicine Lake, ML01 (7.7 g) and ML02 (38.9 g). Fig. 3a shows how the temperature 10 mm within clast ML01 changes during the first 60 s of the experiments. Fig. 3b shows liquid flux (Eq. (3)) as a function of time.
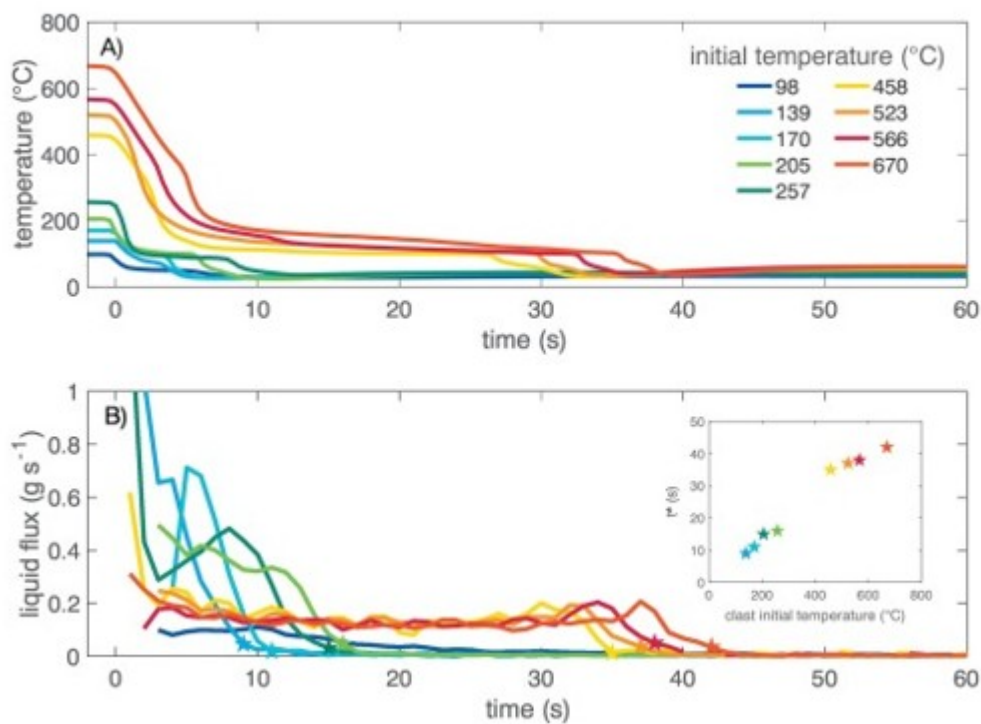

Fig. 3. Effects of initial temperature on cooling and saturation. (A) Internal temperature of clast ML01 as a function of time. Clast internal temperature declines rapidly, approaches 100°C, and finally drops below 100°C. Initially hotter clasts take longer to cool below the phase transition temperature, 100°C. (B) Liquid flux (g s^{-1}) into the clasts as a function of time. Clasts with initial temperatures below 100°C exhibit the lowest liquid fluxes. All clasts with initial temperatures above 100°C exhibit sharp high-to-low liquid flux transitions (Q_l < 0.05 g s^{-1} and marked with stars). The inset shows how the timing of the high-to-low liquid flux transition increases with clast initial temperature.

Several trends are apparent in Fig. 3. First, liquid flux declines sharply in experiments where the initial temperature is greater than the phase change temperature, 100°C. We mark the time, t^*, at which the liquid flux is less than a threshold value, Q_l < 0.05 g s^{-1}. We find that t^* increases with clast initial temperature as illustrated in the inset to Fig. 3b. We find, furthermore, that clast internal temperatures are less than the phase change temperature at t^*.

Second, we observe that the liquid flux before t^* is the same in experiments with initial temperatures ≥ 458°C. This flux is approximately 0.2 g s^{-1} and is less than that observed for initially cooler clasts. Similar results from clast ML02 are shown in Fig. S3.

The observation that clasts with initial temperatures between 139 and 267°C have higher initial liquid fluxes than clasts with initial temperatures ≥ 458°C, suggests that clast thermal energy can impede clast liquid saturation. The observation that liquid flux does not vary with clast initial temperature for temperatures ≥ 458°C suggests that, for these conditions, the pressure gradients driving liquid flow are the same. We note that we cannot observe behaviors of clasts with initial temperatures ≈ 260 − 460°C because our ovens do not operate in this range.

3.3. Conceptual models for pumice cooling and saturation

Here we identify several general behaviors that occur as pumice cool and saturate and we outline these as stages in Table 2 and Fig. 4. We define stage 1 as the stage between pumice submergence and t^*, the high-to-low liquid flux transition (Fig. 4). We define t^* here as the time at which $Q_l < 0.05$ g s^{-1}. Stage 2 follows stage 1 and is the time over which internal temperatures approach ambient. The majority of cooling and saturation occur during stage 1 and we suggest that stage 1 consists of two substages. In this section we describe the processes we hypothesize are important in each stage and substage.

Table 2. Cooling and saturation stages.

Stage and interpretation	Observations	Scaling
(1a) Gas escape controlled: Gas flows out of clasts and liquid water enters. Ingested water is converted to steam in clasts above the boiling temperature.	Visible bubble flow out of the clasts.	For initial temperatures less than the phase change temperature (100°C): $Q_l \propto e^{-\xi t}$
(1b) Heat conduction and steam condensation controlled: Heat loss causes condensation of internal water vapor which further drives liquid infiltration and cooling. Stage 1b ends when all the steam within the clast has condensed and the liquid flux into the clast is small ($Q_l < 0.05$ g s^{-1}). A clast can be partially saturated at the end of stage 1 due to the trapping of non-condensable gas.	We observe few bubbles escaping from the clast. Internal temperatures sometimes plateau at 100°C. Liquid flux is lower for very hot clasts compared to warm clasts (Fig. 3).	$q = 7.5 \pm 0.5 \text{Wcm}^{-2}$ $Q_l = q S a L$
(2) Heat conduction controlled: Clasts cool by conduction. Slow liquid saturation results from thermal contraction of non-condensable gas bubbles. Internal	Submerged weight increases gradually and internal temperatures slowly approach ambient.	$\ln T(r,t)$ $−T∞ Ti − T∞ \propto t$ $Q_l \propto dTdt$

clasts temperatures can increase at the beginning of stage 2 as heat from warm regions of the clast (e.g., the interior or heterogeneous areas) is conducted into colder areas.
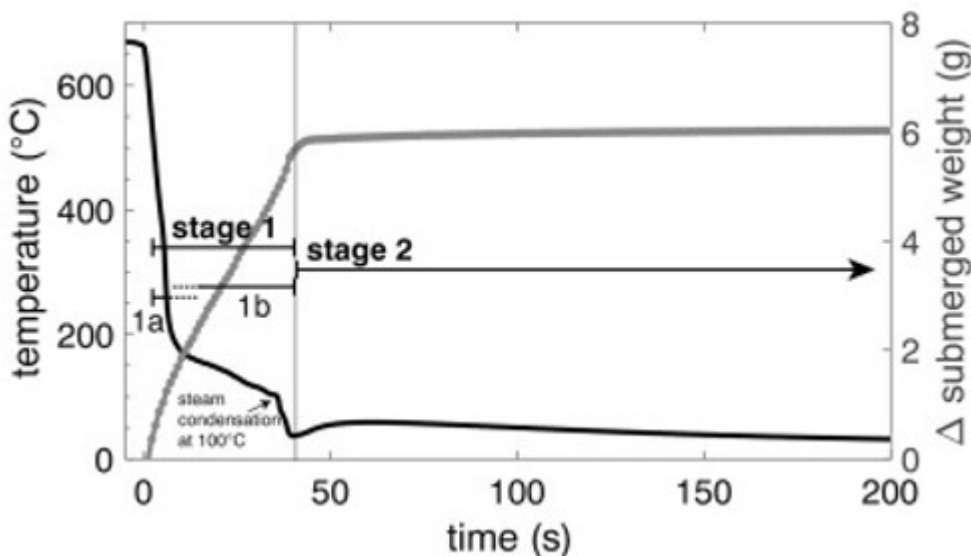

Fig. 4. Cooling and saturation stages of representative clast ML01. We propose that cooling and saturation takes place in several stages and over which different processes dominate. Stage 1a: Water enters the clast as air flows out. If the clast is hot, ingested water is converted to steam. The dashed lines express uncertainty in the stage 1a to 1b transition. Stage 1b: Clast at least partially contains steam. As the clasts cool, internal steam condenses and generates a pressure gradient that draws in liquid water. Stage 1 ends once all internal steam has condensed. Stage 2: Cooling occurs through conduction and saturation is controlled by the thermal contraction of trapped non-condensable gas.

Hot clasts are known to convert ingested water to steam (e.g., Whitham and Sparks, 1986). We define stage 1b as the time over which steam is present within the clasts (Table 2). We further propose that clast cooling causes water vapor condensation and that the associated volume change draws in liquid water. Clasts can contain liquid water, steam, and trapped gas during stage 1b. Whitham and Sparks (1986) proposed a similar connection between pumice cooling and saturation where, "as the pumice cools below 100°C the steam will condense leading to water vapor being adsorbed." Stage 1b is therefore relevant for understanding the behavior of initially steam-filled clasts.

Several experimental observations support the hypothesis that water vapor condensation leads to saturation including: (1) the absence of visible gas escape as submerged weight increases; (2) the observation that the rate of cooling with time increases immediately after internal temperatures fall below 100°C (Fig. 4) - consistent with a condensation-associated volume change drawing cooler water to the thermocouple; and (3) the observation

that very hot > 458°C pumice saturate more slowly than lower temperature pumice (Fig. 3) - suggesting that heat loss impedes saturation.

We suggest that Stage 1b ends when all steam within the clast has condensed. We recognize the end of stage 1, t^*, as the time when liquid flux becomes small ($Q_l < 0.05$ g s^{-1}). However, we note that clasts with initial temperatures < 100°C (the phase change temperature at ambient pressure) do not exhibit an abrupt change in liquid flux and we propose this is because cool clasts cannot generate steam.

Stage 2 begins when once all internal steam has condensed. During stage 2 we expect that clasts contain only liquid water and, possibly, non-condensable gas such as trapped air (Fauria et al., 2017). We hypothesize that heat conduction controls stage 2 cooling and saturation occurs through the thermal contraction of trapped non-condensable gases.

4. Testing concepts for pumice cooling and saturation with quantitative models

We proposed conceptual models for the stages of pumice cooling and saturation in Section 3.3 and Table 2. We test those concepts here by developing process-based quantitative models for the various stages of pumice cooling and saturation that we compare to our experimental results. The clast-scale models developed in Sections 4.1–4.5 match experimental observations - lending confidence to our conceptual understanding and providing quantitative tools to extrapolate to conditions not explored with experiments.

In Sections 4.6–4.7 we combine all our experimental results to derive average clast cooling and saturation rates. These expressions may be useful in submarine plume models and are based on the understanding of clast cooling and saturation developed in Sections 4.1–4.5.

4.1. Stage 1a: saturation of pumice below the phase change temperature

We find that the flux of liquid water into clasts (Eq. (3)) decreases exponentially with time for clasts with initial temperatures less than the boiling point such that

$$(4) Q_l(t) = Q_o \exp(-\xi t),$$

where Q_o is the initial flux of liquid into the clast, ξ is a fitted coefficient, and t is time (Fig. 5). The exponential decline in Q_l is consistent with a Darcy model for flow in which pressure gradients are generated by hydrostatic pressure (Horton 1933; Assouline, 2012). For the same clast, initial liquid flux increases with initial clast temperature (Fig. 5) and we hypothesize that this is because thermal contraction adds to the pressure gradient drawing water into the clast.
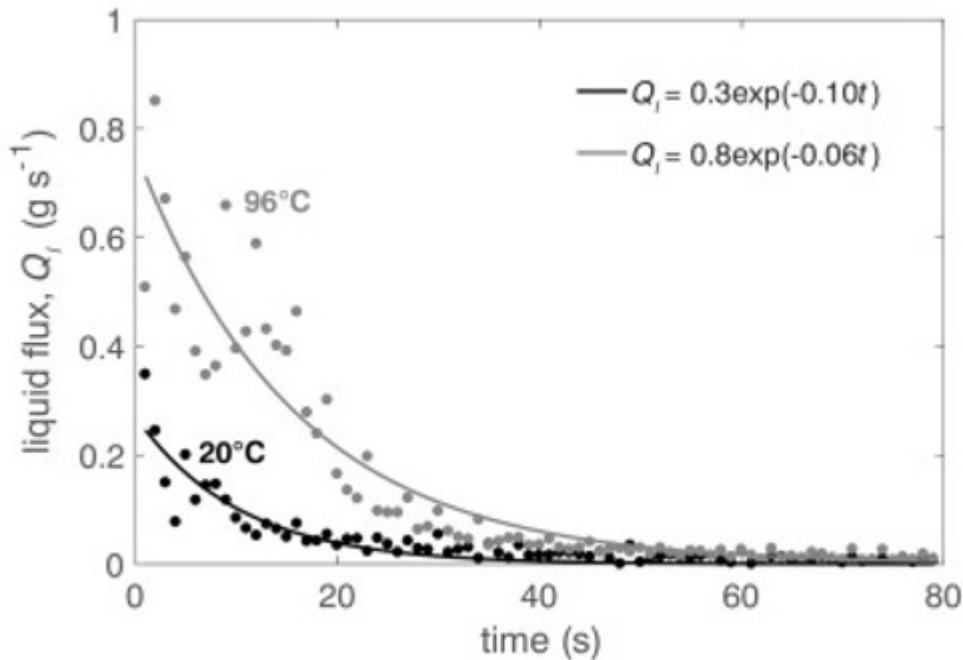
Fig. 5. Flow declines exponentially with time for clasts with initial temperatures < 100°C (the phase change temperature at 1 atm). We fit Eq. (4) to measurements of liquid flux from clast ML02 and find that liquid flux increases with clast initial temperature.

4.2. Stage 1a: saturation of pumice above the phase change temperature

When the initial temperature of a clast is greater than the boiling point, we observe that the initial saturation of the clast is rapid (e.g., Fig. 3). We propose that rapid air escape and water ingestion occur as a result of hydrodynamic instabilities (e.g., Dufek et al., 2007). Thermal contraction of air may also draw in liquid water (e.g., Allen et al., 2008). While stage 1a liquid flux is high, we do not yet have a quantitative model for this stage. We propose, however, that as liquid water is ingested and comes into contact with the hot clast interiors, water is flashed to steam. Stage 1a would not exist for initially water vapor-filled clasts.

4.3. Stage 1b: cooling controls saturation

Stage 1a transitions to stage 1b when clasts contain appreciable steam. During stage 1b, we envision that cooling generates an inward moving condensation front (Fig. 6) and that clasts saturate as condensation draws in liquid water (e.g., Whitham and Sparks, 1986). This scenario is similar to the classic Stefan problem, where heat loss drives the movement of a vapor-liquid interface, except that permeable clasts can ingest water and ingested water may accelerate cooling.
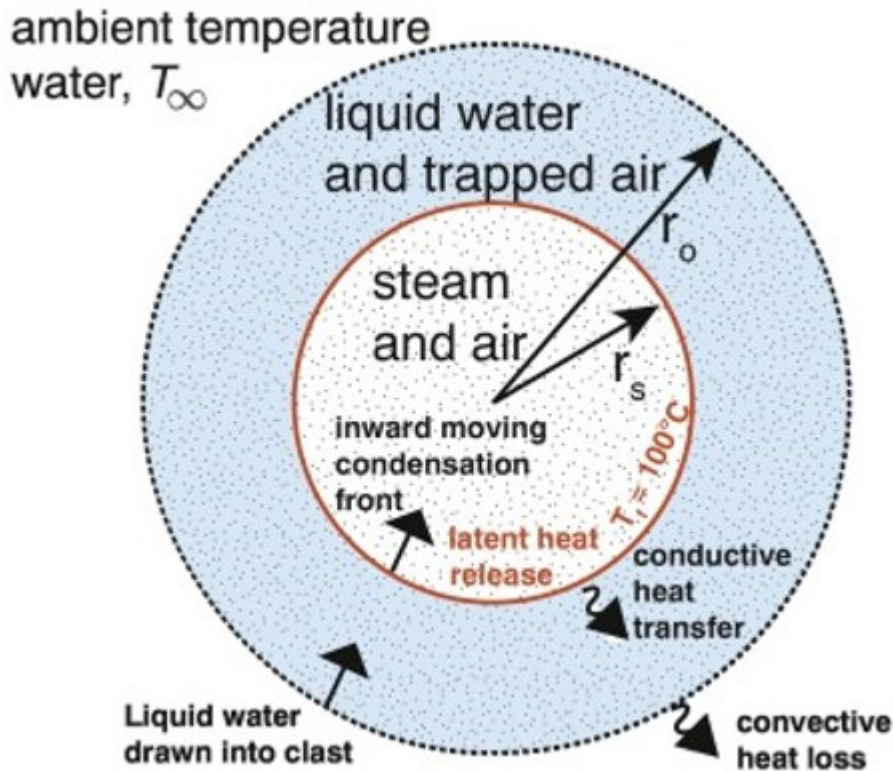
Fig. 6. Conceptual model of stage 1b cooling and saturation. Clasts contain steam in their pores. Internal steam condenses as the clasts cool - generating an inward propagating condensation interface. At the condensation interface the production of latent heat balances outward heat conduction. Liquid water is drawn into the clast at the velocity of the condensation interface. The mathematical details of this model are given in Appendix B.

We compare our experimental measurements against a Stefan model with advection to test the idea that cooling controls the saturation of steam-filled clasts. Because the Stefan model neglects clast permeability, we first argue (Section 4.3.1) why permeability does not limit clast saturation.

4.3.1. Why permeability may not limit clast saturation

Consider a vapor-filled pumice that loses heat to its surroundings (e.g., Fig. 6). Similar to the classic Stefan problem, we expect heat loss to cause condensation and drive the movement of a vapor-liquid interface at velocity *v*. Because pyroclasts are permeable, we also except that liquid water can be drawn into the clast. To determine whether heat loss or permeability limits clast saturation, we compare the velocities at which water flows into a clast as a result of permeable flow versus heat loss. The slowest velocity will limit, and thereby control, clast saturation.

If heat-loss controls flow, the speed of the vapor-liquid interface is determined by the classic Stefan problem (Fig. 6), where heat conduction is balanced by the release of latent heat at the vapor-liquid interface

$$(5) \quad k_{eff} \frac{dT}{dx} = \rho \phi L v,$$

where k_{eff} if effective thermal conductivity, T is temperature, x is distance, v is the velocity of the steam-liquid interface, ρ is the fluid density, L is the latent heat of condensation, and where we assume that all vapor is condensable. For this scaling analysis, we use a steady-state solution to the 1-dimensional advection-diffusion problem (Bredehoeft and Papaopulos, 1965) to estimate the temperature distribution of the liquid-saturated part of the clast

$$(6) \quad \frac{T(x) - T_\infty}{T_i - T_\infty} = \frac{e^{Pe \, x/(r_o - r_s)} - 1}{e^{Pe} - 1}$$

where $r_o - r_s$ is the distance between the edge of the clast and the steam-liquid interface, and $Pe = \frac{v(r_o - r_s)}{D_{eff}}$ is a dimensionless Peclet number (the rate of heat advection to diffusion), and D_{eff} is the effective thermal diffusivity. We solve for the infiltration speed of liquid water, v, into the clast by combining Eqs. (5) and (6)

$$(7) \quad v = \frac{-D_{eff}}{r_o - r_s} \ln \left[1 - \frac{k_{eff}(T_i - T_\infty)}{\rho_s \phi L D_{eff}} \right].$$

Alternatively, if permeability controls saturation clasts saturate at the velocity given by Darcy's law

$$(8) \quad v = \frac{\kappa}{\mu \phi}(\rho_l g - \nabla p),$$

where κ is permeability, μ is water viscosity, $\rho_l g$ is the hydrostatic pressure gradient and $-\nabla p$ accounts for additional pressure gradients. We let $-\nabla p = \frac{P_1}{r_o}$ to account for the pressure gradient induced by condensation (Appendix A).

The lowest velocity derived from either permeable flow (Eq. (8)) or heat transfer (Eq. (7)) will control the pyroclast saturation rate because the slowest process is rate-limiting.

By combining Eqs. (8) and (7), we find that permeability can limit clast saturation if

$$(9) \quad \kappa < \frac{-\mu \phi D_{eff}}{(r_o - r_s)} \frac{\ln\left[1 - \frac{k_{eff}}{T_i - T_\infty} \rho \phi L D_{eff}\right]}{\frac{P_1}{r_o} + \rho_l g}.$$

Given $D_{eff} = D_w \phi + D_r(1 - \phi) \approx 2.5 \times 10^{-7}$ m^{2}s^{-1} for $\phi = 0.7$ (Bagdassarov et al., 1994), $k_{eff} = 1$ W m^{-1}K^{-1}, $T_i - T_\infty = 100 \,^{\circ}$C, $\rho = \rho_l$, and $P_1 = 10^5$ Pa, permeability can limit saturation if $\kappa < 8.5 \times 10^{-16}$ m^2 for $r_o = 2$ m and $r_s = 1$ m or $\kappa < 1.0 \times 10^{-15}$ m^2 for $r_o = 0.02$ m and $r_s = 0.01$ m. Because permeability values in pumice are larger, typically $\sim 10^{-12}$ m^2 (e.g., Klug and Cashman, 1996, Saar and Manga, 1999, Rust and Cashman, 2004, Mueller et al., 2005, Wright et al., 2009, Degruyter et al., 2010, Burgisser et al., 2017, Colombier et al., 2017, Gonnermann et al., 2018), we argue that permeability does not limit clast saturation for both large and small clasts.

In the next section we compare a model for cooling-controlled saturation against observations from a small 1.4 cm diameter clast. We find that a Stefan model with advection, and which neglects permeability, matches observations.

4.3.2. Stefan model with advection

We proposed that stage 1b cooling and saturation are similar to the classic Stefan problem, except that liquid water is drawn into permeable clasts as vapor condenses (Fig. 6). To test the applicability of the classic Stefan problem to hot pyroclasts and to better understand how vapor-filled clasts saturate, we build a Stefan model with advection. We then compare the Stefan model with advection to our experimental results.

The full set of equations for the 1-D Stefan model with an advective component are given in Appendix B. The model is based on a balance between the outward conduction of heat and the production of latent heat from condensation. This balance gives rise to the inward migration of a condensation interface (Fig. 6). We allow liquid water to flow into the clast at the velocity of the condensation interface. As a result, water ingestion can enhance cooling in our model. We also assume that a constant heat transfer coefficient can describe heat loss at the clast's outer boundary and that the clast's steam-filled interior maintains constant pressure of 1 atm and temperature of 100°C. We solve the Stefan problem with advection numerically for both planar and spherical geometries. As described in Section 4.3.1, this model neglects clast permeability because saturation is controlled by heat loss. Furthermore, we use an effective Stefan number because the majority of the thermal mass may be in the rock rather than the steam (Appendix C).

We compare the Stefan model with advection against measured or calculated quantities from our experiments: the condensation front position, the time at which the condensation front reaches the clast center, and the effective Stefan number.

We calculate the condensation front position in our experiments from submerged weight and according to

$$(10) \quad v = \frac{dr_s}{dt} \propto \frac{Q_l(t)}{\rho_l \phi S_{ac}},$$

where v is infiltration velocity, r_s is the condensation front location, ρ_l is liquid density, ϕ is porosity, $S_{ac} = \frac{1}{C_1} 4\pi r_o^2$ is the surface area of the condensation front, C_1 is an empirically determined constant, and $Q_l(t)$ is the calculated liquid flux (Eq. (3)). We assume S_{ac} is constant in Eq. (10) as is the case if pumice saturate like a series of parallel tubes. The time at which the condensation front reaches the clast center is the stage 1 to 2 transition or t^*.

The effective Stefan number expresses the ratio of sensible to latent heat in a clast, is calculated as described in Appendix C, and decreases as clast initial temperature increases. That is, clasts with higher initial temperatures have lower effective Stefan numbers and take longer to cool and saturate. For example, using the values given in Appendix C we find $St_{eff} = 4.9$ and 2.9 for clasts with temperatures of 400 and 600°C, respectively.

We compare numerical solutions to the Stefan model with advection to experimental results (ML01 with $T_i = 523$°C) in Fig. 7. Fig. 7 shows

normalized condensation front position as a function of time. The time at which normalized front position reaches zero is the time at which all internal steam has condensed.
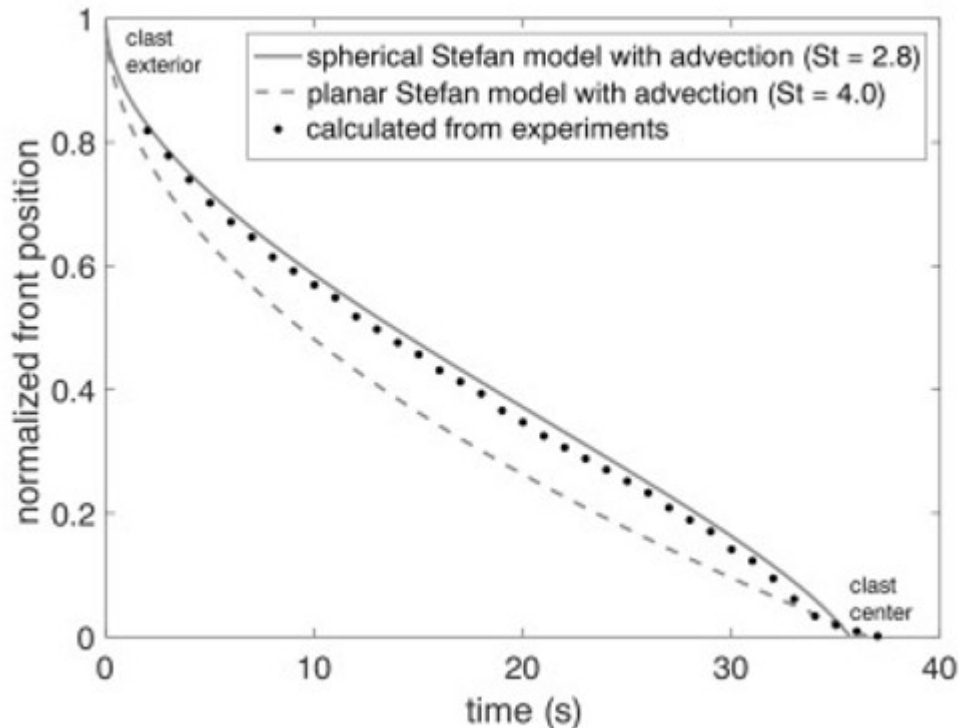

Fig. 7. Normalized condensation front position (rsro) as a function of time. We use our experimental measurements to calculate the condensation front position (Eq. (10) with $C_1 = 2.6$, black circles). The best estimate of St during the experiment is 3.5 (based on equation C.4). We compare calculated front position to solutions from a modified Stefan model in spherical and planar geometries (Appendix B). We find that, using reasonable Stefan numbers, the modified Stefan model matches our experimental measurements, lending support to the conceptual model for stage 1b depicted in Fig. 6.

We find that the Stefan model with advection agrees with experimental results and with similar Stefan numbers (Fig. 7). The agreement between the modeled (Appendix B) and calculated (Eq. (10)) curves for condensation front position in Fig. 7 lends support not only to the applicability of a Stefan model with advection to pumice, but to the concept that pyroclast cooling controls saturation.

We emphasize that the Stefan model with advection, while simulating the behavior of steam-filled pumice, matches the saturation behavior of initially air-filled clasts. This similarity exists because ingested liquid water is efficiently vaporized to steam (Eqs. (C.2) and (C.3)). That is, only a small fraction of glass thermal energy is required to convert ingested liquid water to steam because there is much more thermal energy in a clast's glass matrix compared to (pore-filling) water vapor.

Non-condensable gases (such as air) may become trapped as air-filled clasts saturate. We account for the presence of trapped gas with the term g_f in Eq.

(C.4). Future work may examine the role of trapped non-condensable gas pockets in cooling and saturation dynamics.

4.4. Stage 2 cooling by conduction

Stage 2 begins once all internal steam has condensed and, as a result, the liquid flux declines below a threshold value (e.g., Fig. 3). We propose that stage 2 heat loss is dominated by conduction, rather than advection. To test this hypothesis, we compare stage 2 temperature measurements to solutions of a heat conduction model on a sphere (Appendix D). To model stage 2 cooling we assume: (1) pumice is spherical; (2) the clast has a uniform initial temperature T_i; (3) clast internal structure is uniform; (4) the clast's convective heat flux is uniform with heat transfer coefficient H; (5) the water bath has constant temperature $T\infty$; (6) all pumice pores are filled with liquid water; and (7) heat is transferred by conduction inside the clast.

The Biot number expresses the ratio of internal to external resistance to heat transfer and is

$$(11) \quad Bi = \frac{H r_o}{k_{eff}},$$

where H is the heat transfer coefficient, r_o is the clast radius and k_{eff} is effective thermal conductivity. A Biot number ≤ 0.1 implies that heat loss is limited by external heat transfer and the temperature within the clast is approximately uniform. Because we find that clast internal temperature is spatially variable during stage 2 (e.g., Fig. 2) we expect that $Bi \geq 0.1$ and therefore a lumped capacitance model is not suitable.

The exact solution for the time dependent non-dimensionalized radial temperature distribution (Appendix D) across a conductive sphere with a convective boundary layer is

$$(12) \quad \theta(r,t) = \frac{(T(r,t) - T\infty)}{(T_i - T\infty)} = \sum_{n=1}^{\infty} A_n \exp(-\lambda_n^2 \tau) \frac{\sin \lambda_n \frac{r}{r_o}}{\lambda_n \frac{r}{r_o}},$$

where $\theta(r,t) = \frac{(T(r,t) - T\infty)}{(T_i - T\infty)}$ is dimensionless temperature, r is clast radial position, $\tau = \frac{D_{eff} t}{r_o^2}$ is non-dimensionalized time and D_{eff} is effective thermal diffusivity, $A_n = \frac{4(\sin \lambda_n - \lambda_n \cos \lambda_n)}{2\lambda_n - \sin 2\lambda_n}$ and the values for λ_n are the positive roots of the transcendental equation $Bi = 1 - \lambda_n \cot(\lambda_n)$ (e.g., Incropera et al., 2002).

The solution to Eq. (12) can be approximated with the first term of the series for $\tau > 0.2$ (Incropera et al., 2002) such that

$$(13) \quad \theta(r,t) = \frac{(T(r,t) - T\infty)}{(T_i - T\infty)} = A_1 \exp(-\lambda_1^2 \tau) \frac{\sin \lambda_1 \frac{r}{r_o}}{\lambda_1 \frac{r}{r_o}},$$

where A_1 and λ_1 are determined for different Biot numbers (Schneider, 1955). Eq. (13) shows that the time dependence of temperature is the same at any radial position in the clast such that $\ln(\theta(r,t)) \propto \tau$. Fig. 8 demonstrates how Eq. (13) scaling matches stage 2 temperature measurements.
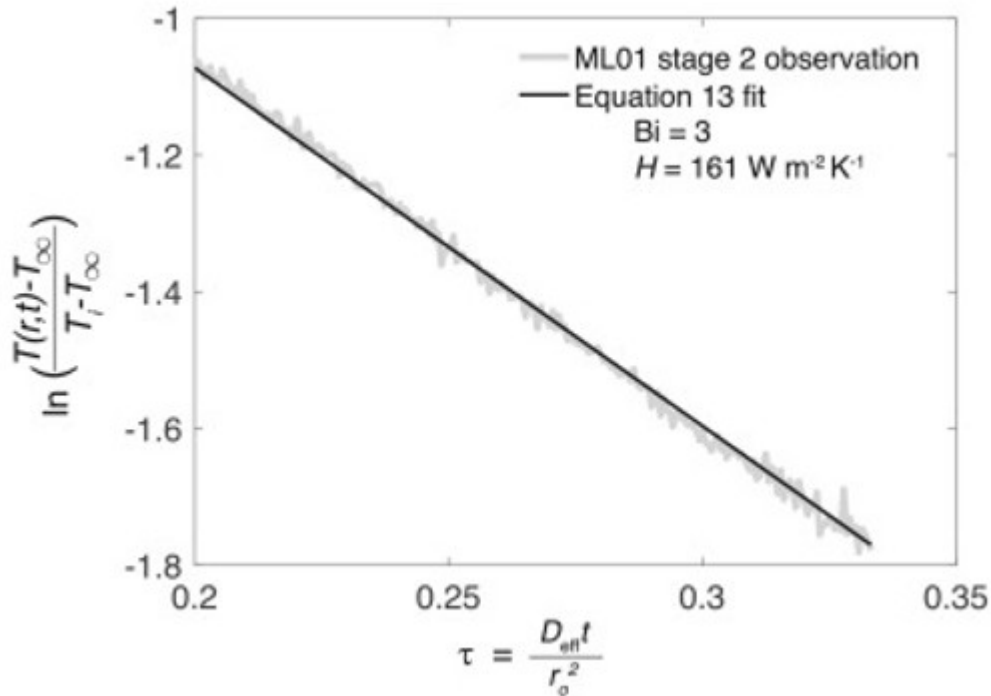
Fig. 8. Stage 2 temperature as a function of dimensionless time, τ. We find that dimensionless temperature scales with $e^{-\tau}$, supporting the concept that clasts cool through conduction during stage 2. We fit conduction model solutions on a sphere (black line) to our experimental measurements to estimate Biot numbers and heat transfer coefficients. See Table 1 for a list of fitted Bi and H values.

We fit Eq. (13) to our experimental measurements to determine Bi and then calculate H. To fit our data we approximate $r_o = \frac{4}{3}\pi V_T^{1/3}$, where V_T is the clast volume. We estimate r from the depth of the hole drilled for each thermocouple (r_t, Table 1). We use the maximum temperature measured during stage 2 to estimate T_i and to set the temporal location where $\tau = 0$. We neglect the temperature dependence of thermal diffusivity and conductivity and calculate effective thermal diffusivity as in Section 4.3.2. Similarly, we estimate effective thermal conductivity according to $k_{eff} = k_w\phi + k_r(1-\phi) \approx 0.7$ W m^{-1}K^{-1}, where k_w is water thermal conductivity and k_r is rock thermal conductivity.

We iteratively find the Biot number that fits Eq. (13) to our temperature measurements for $\tau > 0.2$. Fig. 8 shows how Eq. (13) matches our data and based on the fit we estimate Bi and H (Table 1). We find Biot numbers and heat transfer coefficients in the range of $1-10$ and $20-350$ W m^{-2}K^{-1}, respectively (Table 1). By comparison, typical heat transfer coefficients are lower for pyroclasts cooling in air, ≈ 15 W m^{-2}K^{-1} (Stroberg et al., 2010) and much higher for steel, nickel, aluminum, and copper cooling in water, $\approx 10^3 - 10^4$ W m^{-2}K^{-1}, with H decreasing with the surface temperature of the metal (Bamberger and Prinz, 1986).

4.5. Stage 2 saturation by thermal contraction

During stage 2 we find that clast submerged weight changes linearly with temperature (Fig. 9). We propose that the linear relationship in Fig. 9 reflects thermal contraction of internal fluids (primarily trapped air) and consequent ingestion of liquid water. That is, the total amount of trapped gas is conserved and the amount of liquid water increases as water fills the space made available by thermal contraction.
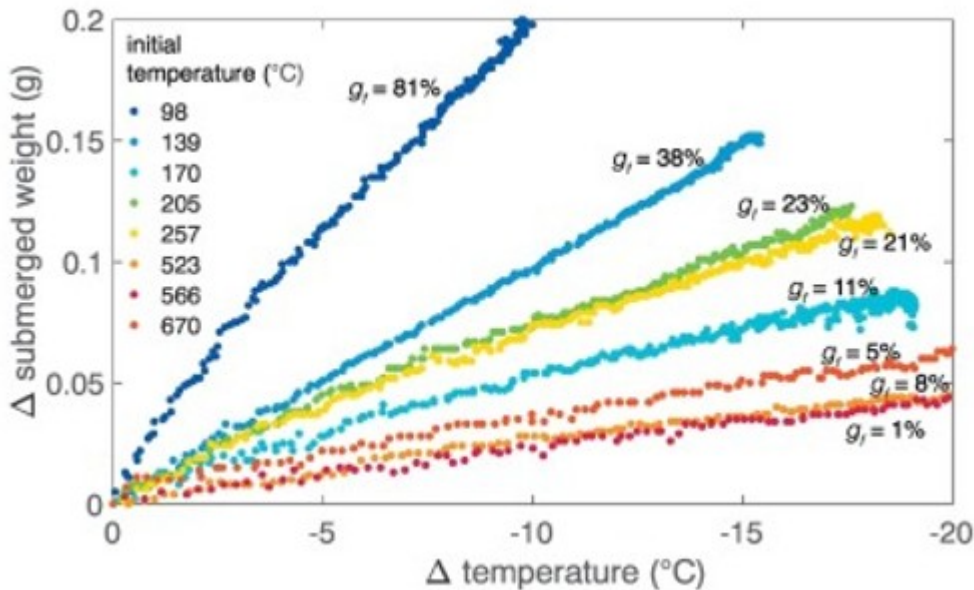

Fig. 9. Stage 2 saturation of clast ML01. Submerged weight increases linearly as temperature declines during stage 2. The linear relationships between submerged weight and temperature indicate that the clast saturates as thermal contraction draws in liquid water during stage 2. We propose that $\Delta MS \Delta Tr$ increases with trapped gas content and use Eq. (16) to solve for trapped gas content, g_f. We find that trapped gas content generally decreases as clast initial temperature increases.

At constant pressure, the volumetric coefficient of thermal expansion

$$(14)\quad \alpha = \frac{1}{V_f}\frac{dV_f}{dT},$$

demonstrates that fluid volume changes linearly with temperature, where V_f is fluid volume. Because the thermal expansion coefficient of air is an order of magnitude greater than that of water, clasts that contain more trapped air (or trapped non-condensable magmatic gases) will contract more and ingest more water more per degree of cooling such that

$$(15)\quad \frac{dM_T}{dT_r} \propto g_f,$$

where T_r is the internal temperature at any radial position and $g_f = \frac{V_g}{\phi V_T}$ is the fraction of trapped gas within the pore space (Fauria et al., 2017). Appendix E shows how the change in submerged weight with temperature depends on trapped gas volume,

$$(16)\quad \frac{dM_T}{dT_r} = -V_T\phi\rho_l[\alpha_l - g_f\alpha_l + g_f\alpha_g],$$

where α_l and α_g are the thermal expansion coefficients for liquid water and air, respectively. Eq. (16) includes effects from both liquid water and air contraction.

Fig. 9 demonstrates how clast submerged weight scales linearly with temperature during stage 2. In Fig. 9 we define $\Delta M_s = M_s(t) - M_s(t_{s2})$ and $\Delta T_r = T_r(t) - T_r(t_{s2})$ where t_{s2} is a time soon after the beginning of stage 2 (specifically t_{s2} is 30 s after the observed temperature maximum in stage 2).

We find that dMTdTr, and thus trapped gas fraction g_f generally decrease with increasing clast initial temperature. The observation that initially hotter clasts trap less gas is consistent with previous work which shows that trapped gas fraction decreases with increasing clast initial temperature (Allen et al., 2008, Fauria et al., 2017, Manga et al., 2018).

4.6. Clasts cool at the same average rate

Observations of liquid flux as a function of time show that the length of time until the stage 1 to stage 2 transition, t^*, increases as clast initial temperature increases (Fig. 3). Here, based on results from all experiments, we propose that t^* increases linearly with clasts' initial thermal energy (Fig. 10). An increase in t^* with clast initial thermal energy is consistent with the idea that clasts must cool below the boiling point to condense all internal steam and transition to stage 2.
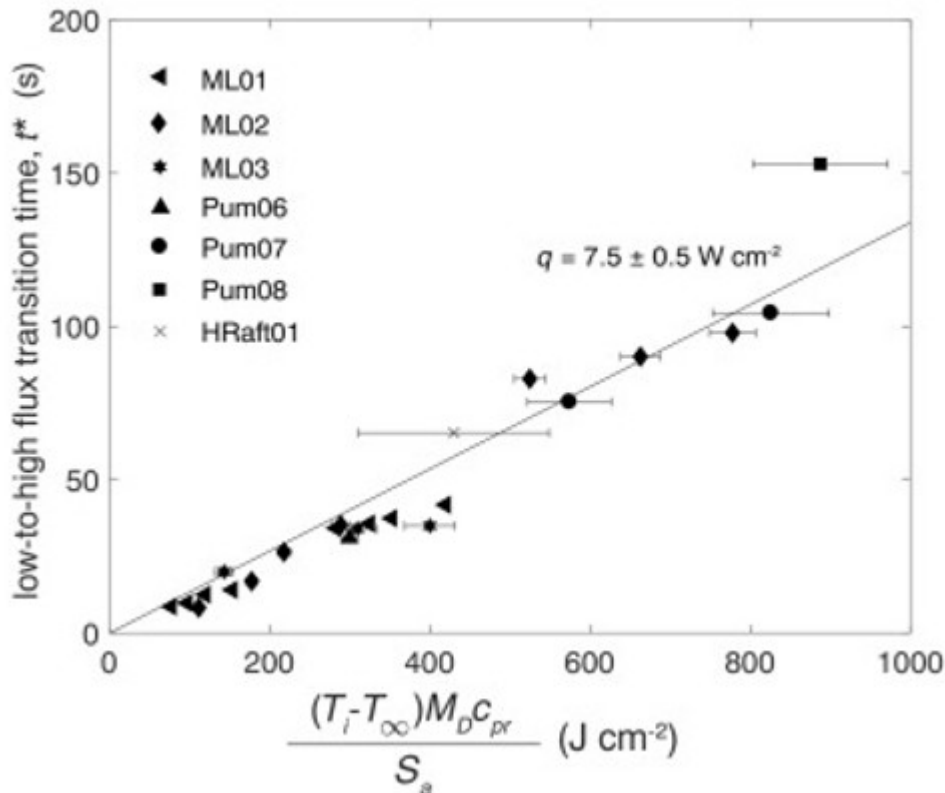

Fig. 10. High-to-low liquid flux transition, t^*, as a function of clast initial thermal energy and surface area. Consistent with our concept that clasts must lose a sufficient amount of thermal energy to condense all internal steam and reach t^*, the linear relationship indicates that clasts experience the same time-integrated average rate of heat loss, $q = 7.5 \pm 0.5$ W cm^{-2}.

We plot t^* as a function of clast initial thermal energy divided by clast surface area in Fig. 10. Fig. 10 shows a linear relationship that can be approximated by

$$(17)\quad \underset{\text{cooling time}}{t^*} = \underset{\text{average heat flux}}{\frac{1}{q}} \underset{\text{initial heat content}}{\frac{(T_i - T_\infty)c_{pr}M_D}{S_a}},$$

where q is a fitted coefficient that represents heat flux in $W\,cm^{-2}$, c_{pr} is the heat capacity of the solid phase, M_D is clast dry mass, and S_a is clast surface area. The linear scaling in Eq. (17) implies that the stage 1 to 2 transition occurs when a sufficient amount of heat has been lost and suggests that the clasts of different sizes, porosities, and initial temperatures, experience the same average heat flux during stage 1 such that q is the same for different clasts. From Fig. 10, we estimate $q = 7.5 \pm 0.5\ W\,cm^{-2}$.

Because we could not measure the submerged weight of very large clasts, we used high speed video and temperature measurements to determine t^* for these clasts (Pum07, Pum08, and HRaft01). Uncertainty in the surface area of the clasts generates the largest uncertainty in the right side of Eq. (17) and therefore q. We approximate surface area by letting S_a be the average of the spherical equivalent surface area and the elliptical equivalent surface area, $S_{a\,ellipsoid} = 4\pi \left(\frac{(r_1 r_2)^{1.6} + (r_2 r_3)^{1.6} + (r_2 r_3)^{1.6}}{3} \right)^{\frac{1}{1.6}}$, where r_1, r_2, and r_3 are the axes dimensions that we measure on each clast (Fig. S4).

The t^* timescale is significant because it represents the time over which a clast is at least partially above the boiling point and contains steam. The result that different clasts have the same average stage 1 heat flux may be useful in models of pyroclast dispersal and clast buoyancy evolution (e.g., Manga et al., 2018). We note that t^* measured on a clast from the 2012 submarine eruption of Havre volcano (HRaft01) follows the same trend as the other clasts.

Extrapolation of $q = 7.5 \pm 0.5\ W\,cm^{-2}$ to much larger clast sizes should be done with caution, however. Heat loss may be slower in very large clasts because temperature gradients may be smaller.

4.7. A new model for clast saturation: a balance between condensation and water ingestion

We observe that liquid flows into clasts at the same rate for very hot clasts and that the liquid flux is relatively constant through time during stage 1 (Fig. 3). Here we propose a method to estimate the average stage 1 liquid flux, Q_l, based on our findings that saturation is governed by heat loss and that there is an average rate of heat loss, $q = 7.5 \pm 0.5\ W\,cm^{-2}$. Specifically we propose

$$(18)\quad Q_l = \frac{q S_a}{L},$$

where S_a is the clast surface area, and L is the latent heat of condensation. Eq. (18) reflects a balance between the rate of liquid flow coming into the clast (lhs) and the rate of condensation (rhs). Eq. (18) does not include thermal contraction effects or account for the presence of non-condensable

gas. Eq. (18) assumes that clasts are at constant pressure and near the phase change temperature such that any cooling generates condensation.

We compare Eq. (18) to average stage 1 saturation rates (measured for clasts with initial temperatures > 458°C) in Fig. 11. We do not report saturation rates for our largest clasts (Pum 07, Pum08, and HRaft01), because these clasts were too buoyant in water to measure their submerged weight with our set-up.
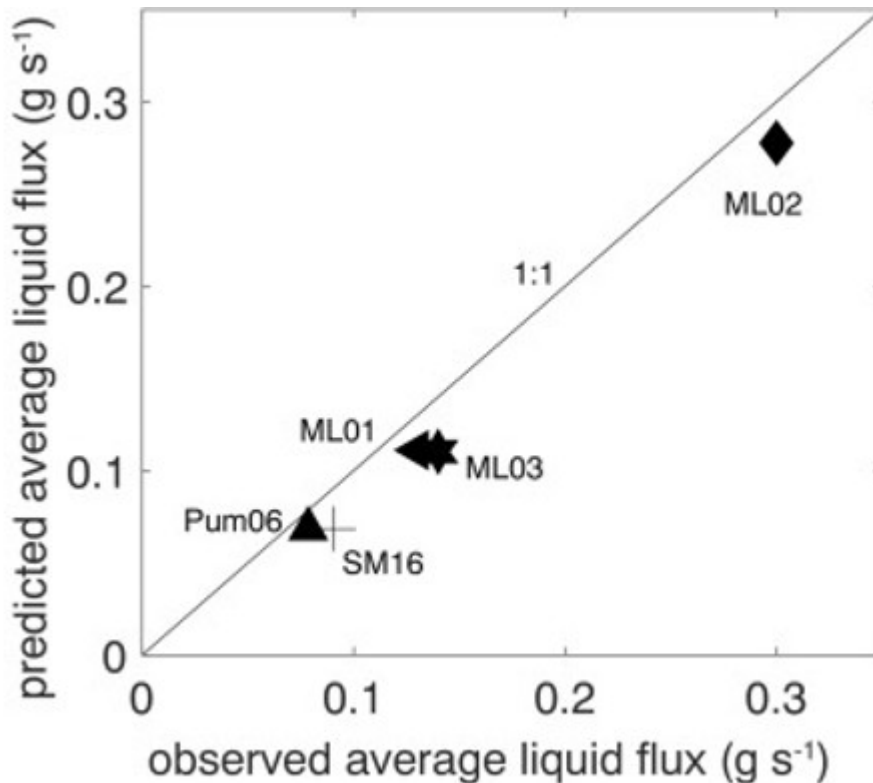

Fig. 11. Observed time-averaged liquid flux versus modeled time-averaged liquid flux (Eq. (18)). We propose that, because Q_l predictions are close to observed values, that we can use Eq. (18) to estimate average rates of liquid flow into clasts and where liquid flow balances steam condensation. The line is 1:1.

We find that Eq. (18) predicted saturation rates, where we use $q = 7.5 \pm 0.5$ W cm^{-2} and S_a as described in Section 4.6, are close to the average stage 1 saturation rates measured in our experiments (Fig. 11).

Eqs. (17) and (18) may prove useful in models of submarine pyroclast dispersal because they provide a way to estimate average saturation and cooling rates based on measurable quantities such as clast porosity, size, and initial temperature. Because we did not validate Eq. (18) on clasts larger than 5 cm diameter, extrapolation to larger clast sizes should be done with caution.

5. Discussion

In the preceding sections we presented observations of, and quantitative models for, pumicecooling and saturation. We found that pumice containing

steam and trapped air cools in two-stages. In stage 1, water ingestion both accelerates, and is limited by, clast cooling. We argued that during stage 1b heat transfer, rather than permeability, controls saturation and tested this idea with a Stefan model with advection. We proposed that stage 2 cooling and saturation are controlled by conduction and thermal contraction, respectively. Finally, we argued that the stage 1 to stage 2 transition occurs when sufficient thermal energy is lost, all vapor has condensed to liquid, and proposed a model to estimate the transition timescale, t^*, as well as average rates of heat loss, q, and liquid water saturation, Q_l.

Here we discuss how the Section 4 models can be applied to submarine eruptions and the limitations associated with extrapolation to parameter spaces not explored in this study but that are relevant for the submarine environment.

5.1. Experimental and model limitations

Submarine pyroclast-generating eruptions differ from the experiments presented here in many important ways. Submarine eruptions often occur in cold, salty, and deep water where high pressures affect gas density, and phase change temperatures. Magmatic volatiles initially fill the pores of submarine-erupted pumice and the type of gas matters because steam condenses while CO_2 (or air) contracts with cooling. Submarine-erupted pyroclasts may form eruption columns (e.g., Kano et al., 1996) or rise as individual clasts (e.g., Rotella et al., 2013) and the development of conceptual models for submarine eruptions is an active area of research (White et al., 2015) that the present study may inform.

Our experiments and models specifically address our understanding of clast rise through the water column and heat transfer from pyroclasts. Yet by neglecting pressure effects in this study we were unable to account for vapor expansion due to decompression or changes in phase change temperature. Because clasts may be able to vesiculate during rise through the water column (e.g., Mitchell et al., 2018), clast permeability and vesicularity may not be static as we assumed.

We conducted experiments on air-filled pumice while submarine-erupted pumice contain primarily water vapor. Because hot air-filled pumice generate steam in their pores when submerged in water (Section 3.3), we use models (Section 4.3) to extrapolate our results to steam-filled pumice. This extrapolation should be done with caution because we were not able to examine the behavior of large, > 10 cm diameter clasts, with experiments. In addition, we did not explicitly model the time-varying and heterogeneous distribution of non-condensable gases in pumice pores nor did we explicitly consider multiphase effects such as liquid and vapor counter flows. Liquid water infiltration may also not be spatially uniform as assumed in our models.

While we estimated an average heat flux for pyroclasts (Sections 4.6), this flux is likely not constant over time. We speculate that in clasts much larger than those examined here ($\gg$ 10 cm diameter), the average heat flux could be less than we measured (7.5 W cm^{-2}) because temperature gradients may be small.

Our experimental set-up precluded the examination of many of the processes listed above. Consideration of these and other processes is needed, however, to model submarine eruption columns (White et al., 2015). Efforts are underway to understand clast rise through the water column by coupling pumice buoyancy evolution to clast vesiculation and an ascent model (Cahalan and Dufek, 2017). The present experimental data may prove useful to validate such numerical models.

5.2. Application to submarine eruptions

Our models for pyroclast cooling and saturation can inform our understanding of submarine eruptions, in particular eruptions that produce pumice rafts or large clasts like the 2012 eruption of Havre submarine volcano (Carey et al., 2018). In submarine pyroclast-producing eruptions, pumice can remain buoyant long enough to reach the ocean surface (e.g., Allen and McPhie, 2009, Barker et al., 2012, Rotella et al., 2013 or may sink part way through the water column (e.g., Kano et al., 1996, Head and Wilson, 2003, Woods, 2010. We note that high porosity subaqueous clasts can be created through both explosive fragmentation or brittle fracture associated with quenching (e.g., Manga et al., 2018). Clasts that reach the surface can enter pumice rafts that are dispersed great distances.

Here we build a model for pumice rise to the ocean surface based on the buoyancy of individual clasts. We use Eq. (18) to determine how pumice buoyancy evolves with time. We then calculate clast rise speeds and determine minimum clast sizes that can reach the surface from 1000 m depth.

To model clast rise, we assume that clasts saturate as a result of heat loss, contain only condensable vapor at the phase change temperature, and the internal vapor does not expand due to decompression. To determine the time until neutral buoyancy we first calculate the fraction of pore space filled with liquid water, ω, as a function of time

$$(19) \quad \omega(t) = \frac{Q_l t}{\phi \rho_l V T},$$

where we use Eq. (18) to estimate Q_l. We calculate clast density, ρ_c according to

$$(20) \quad \rho_c(t) = (1-\phi)\rho_r + \phi\omega(t)\rho_l$$

and determine the water saturation, w^*, at which clasts reach neutral buoyancy (dashed line) such that $\rho_c = \rho_l$ (Fig. 12). Fig. 12 shows how buoyancy time increases with clast size and porosity. We assume that the ambient fluid has a constant density, ρ_l, that does not change with depth or

due to heating. We find that a 0.5 m and 80% porosity clast will remain buoyant for ≈ 20 min and 1 m diameter and 65% porosity clast will remain buoyant for ≈ 12 min. Because Eqs. (18)–(20) do not include the effects of vapor expansion associated with decompression, we expect that the buoyancy times plotted in Fig. 12 represent lower bounds on the longevity of clast rise through the water column.
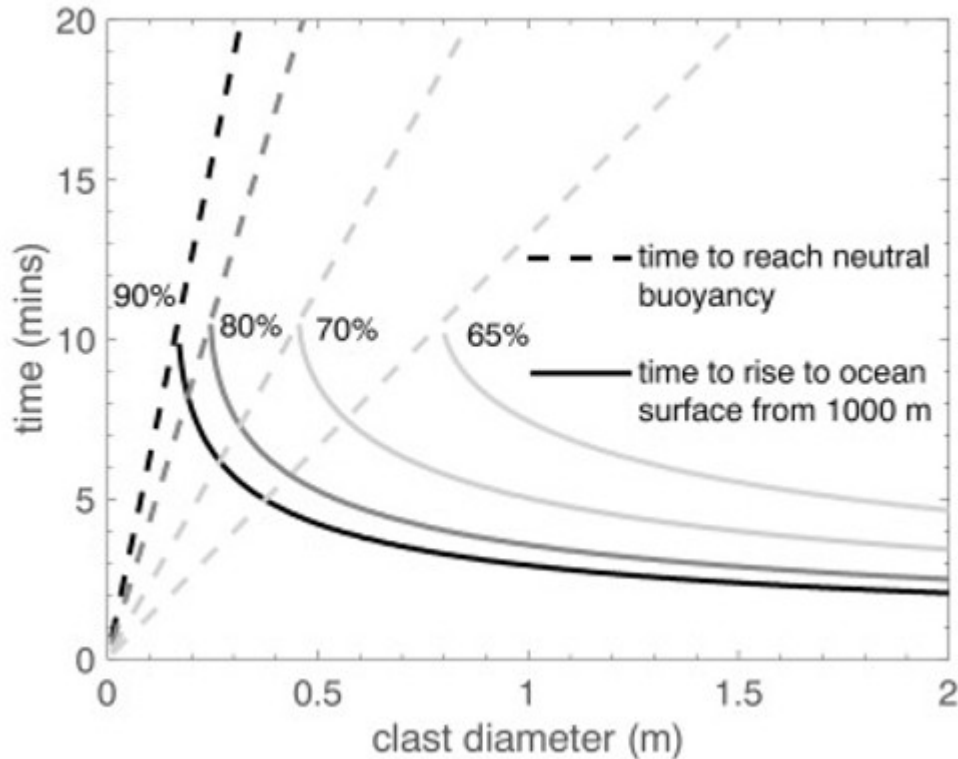

Fig. 12. Clast rise to the ocean surface. Time for a clast to reach neutral buoyancy (dashed lines) and time to rise to the ocean surface from 1000 m depth (solid lines) as functions of clast size and porosity. We model clast saturation as a function of heat loss and steam condensation (Eqs. (18)–(20)). We estimate clast rise times using Eq. (20)–(22). From this figure, we can estimate how long a water-vapor filled clast will remain buoyant (excluding the effects of decompression and vapor expansion) and minimum clast sizes required to reach the surface (intercepts of dashed and solid lines). Porosities are listed in percent.

We compare clast buoyancy times to clast rise times to the ocean surface from a depth of 1000 m (Fig. 12). We estimate clast rise velocities, u, according to

$$(21) \quad u = \sqrt{\frac{8(\rho_l - \rho_c(t))g r_o}{3\rho_l C_d}},$$

and rise distance as

$$(22) \quad L_{rise} = \int u \, dt,$$

where ρ_c is clast density, ρ_l is liquid water density, g is gravity, r_o is clast radius, and $C_d = 0.3$ is a drag coefficient (Batchelor, 1970). By combining Eqs. (20)–(22) we determine the time at which a clast saturating at rate, Q_l would reach the surface from 1000 m depth (Fig. 12).

Fig. 12 shows how, based on Eqs. (19)–(22), we can determine minimum clast sizes required to reach the surface from a depth of 1000 m: 0.8, 0.45, 0.25, and 0.16 m diameter clasts for porosities of 0.65, 0.7, 0.8, and 0.9, respectively (intercepts of dashed and solid lines). Regardless of clast size and porosity, a clast can rise from a depth of 1000 m for ≈ 10 min before either reaching the surface or starting to sink (Fig. 12).

Once pyroclasts reach the surface they can float and form pumice rafts as a result of non-condensable gas trapping (Fauria et al., 2017) and thus have the potential to be dispersed long distances. When clasts reach the surface full of steam, floatation requires that air enters the pore spaces before the clasts cool (e.g., Fiske et al., 2001). Our model supports arguments and observations that large clasts waterlog last and are sometimes able to reach the surface (e.g., Kano et al., 1996, Allen and McPhie, 2000, Stewart and McPhie, 2004, Allen and McPhie, 2009, Cas and Giordano, 2014, and also provides quantitative constraints on the timing of saturation. The recent 2012 eruption of Havre submarine volcano demonstrates how porous volcanic material can be partitioned into both floating and sinking components (Carey et al., 2018) and our model may be useful for understanding those sorting processes.

Conceptual models have also attributed the buoyancy of pyroclasts to steam sheaths that develop around their exteriors. We did not observe, however, steam sheaths in any of our experiments because liquid water can enter the pores and cool the surface below the boiling temperature. Rather, we propose that steam occupies the clast interiors - the warmest regions of the clasts.

Together, our experimental results and models suggest that, because saturation is limited by cooling and condensation, pyroclasts often remain hot and buoyant long-enough to reach the surface. Our clast-scale cooling and saturation models provide tools for understanding the eruption dynamics of events such as the 2012 eruption of Havre volcano - noting that additional physics, such as the effects of pressure changes, should be better resolved to fully understand the evolution of clast buoyancy.

6. Conclusions

Pyroclast cooling and saturation are important for understanding submarine eruption dynamics and pyroclast dispersal. In this study we used laboratory experiments to examine, and develop models for, clast-scale cooling and saturation processes.

We found that pumice cool and saturate in several stages (Fig. 4). At first (stage 1a), gas bubbles flow out as water enters the clasts. Air-filled clasts below the boiling temperature saturate according to Darcy's law where permeability matters (Section 4.1). By comparison, hot clasts convert ingested water to steam and heat loss, rather than permeability, controls vapor-filled clast saturation (i.e., stage 1b, Section 4.3).

We observed that the rate of liquid saturation declines abruptly in hot clasts - indicative of the time, t^*, at which all internal vapor has condensed. We demonstrated that clasts cool by conduction and saturate due to the thermal contraction of trapped non-condensable gasonce all vapor has condensed (i.e., stage 2, Sections 4.4 and 4.5).

Because internal vapor condensation requires the loss of a sufficient amount of heat, we derived an average rate of heat loss for all clasts based on a linear relationship between $t^*$and clast initial thermal energy (Section 4.6). That is, t^* scales lineally with clast initial thermal energy, demonstrating that clasts tested here lose heat at the same time-integrated average rate of $q = 7.5 \pm 0.5$ W cm^{-2}.

We then derived an expression for the average rate of clast saturation (Eq. (18)), based on our finding that the rate of liquid water ingestion balances the rate of condensation in steam-filled pyroclasts (Fig. 11).

Finally, we applied our understanding that heat loss controls steam-filled pyroclast saturation to estimate the time it takes clasts to reach the ocean surface from 1000 m depth (Section 5.2). We find that clasts larger than ~ 1 m diameter can rise to the ocean surface from 1000 mbsl due to their buoyancy and before water-logging. We find that cooling can make small clasts condense internal water vapor, become water-logged and sink before reaching the ocean surface (Fig. 12).

While our experiments and models do not incorporate all the processes relevant for submarine eruptions (e.g., decompression effects) they can provide insight into submarine eruption dynamics. For example, we find that steam-filled pyroclast saturation depends on heat loss, rather than permeability, and this implies that water-logging may be independent of the details of internal texture. In addition, the clast-scale models developed here can inform multiphase models of submarine eruption columns and pyroclast dispersal. Our experimental results may also help validate models that include important processes neglected in this study. In general, our study results support what was already acknowledged - that large and hot pyroclasts saturate slowly as they cool (e.g., Kano et al., 1996, Cashman and Fiske, 1991, Fiske et al., 2001, Allen and McPhie, 2009, Cas and Giordano, 2014, White et al., 2015. The models and data presented here provide a quantitative framework, however, for understanding the mechanics of cooling and saturation and demonstrate that high porosities and phase-changes lead to complex behaviors.

Acknowledgments

Appendix A. Pressure gradient caused by condensation

Here we estimate the pressure gradient generated by condensation in 1-D (i.e., inward movement of a condensation interface). Consider the change in pressure generated by losing n moles of gas from a container or pyroclast. From the ideal gas law

$$(A.1) \quad P_1 n_1 = P_2 n_2,$$

where P is gas pressure, the subscripts 1 and 2 refer to initial and final time, respectively, and where volume and temperature are constant. Assuming that the concentration of moles of gas per unit length is constant, C [moles m^{-1}], we can write $n_1 = C r_o$ and $n_2 = C r_s$ in 1-D and where r_o is pyroclast radius and r_s is the condensation interface position. That is, the number of moles of gas decreases due to condensation where r_s is the location of the condensation interface.

We can substitute into Eq. (A.1) to solve for the pressure difference

$$(A.2) \quad P_2 - P_1 = \Delta P = -P_1 \frac{r_o - r_s}{r_o}.$$

The pressure gradient from the clast edge to the condensation interface becomes

$$(A.3) \quad \nabla p = \frac{\Delta P}{r_o - r_s} = -\frac{P_1}{r_o}.$$

We therefore find that pressure gradients generated by condensation are inversely proportional to clast radius and are the largest in small clasts.

Appendix B. Stefan problem with advection

Here we write the governing equations for the inward propagation of a condensation front in a conductively cooling sphere (e.g., Pedroso and Domoto, 1973, Riley et al., 1974, Ismail and Henrıquez, 2000 and with an advective term to account for water flow into the clasts. Consider a sphere of radius r_o composed of a homogeneous fluid with initial temperature T_f, where T_f is the phase change temperature, and surrounded by a bath of subcooled fluid of constant temperature $T\infty$ (Fig. 6). We write 1-dimensional equations that govern sphere cooling by conduction and advection and propagation of an internal condensation front as:

$$(B.1) \quad \frac{\partial T}{\partial t} = D_{eff} \left(\frac{2}{r} \frac{\partial T}{\partial r} + \frac{\partial^2 T}{\partial r^2} \right) - \frac{\partial r_s}{\partial t} \frac{\partial T}{\partial r} \bigg|_{r_s < r < r_o}$$

$$(\text{B.2})\quad k_{eff}\frac{\partial T}{\partial r}=\rho_{eff}L_{eff}\frac{\partial r}{\partial t}\Big|_{r=r_s}$$

$$(\text{B.3})\quad T=T_f\,|_{r<r_s}$$

$$(\text{B.4})\quad -k_{eff}\frac{\partial T}{\partial r}=H(T-T_\infty)\,|_{r=r_o}$$

$$(\text{B.5})\quad T(r,0)=T_f$$

where k_{eff} is effective thermal conductivity, $r_s(t)$ is the position of the phase change front, ρ_{eff} is effective density, L_{eff} is effective latent heat, and H is the heat transfer coefficient. We use effective latent heat to account for multiphase effects (Appendix C). By defining the following dimensionless variables $\tau=\frac{D_{eff}t}{r_o^2}$, $R^*=1-\frac{r}{r_o}$, $S=1-\frac{r_s}{r_o}$, $\theta(r,t)=\frac{(T(r,t)-T_\infty)}{(T_f-T_\infty)}$, $St=\frac{c_{p,eff}(T_f-T_\infty)}{L_{eff}}$, and $Bi=\frac{Hr_o}{k_{eff}}$, we can write the model equations as

$$(\text{B.6})\quad \frac{\partial \theta}{\partial \tau}=\frac{2}{R^*-1}\frac{\partial \theta}{\partial R^*}+\frac{\partial^2 \theta}{\partial R^{*2}}-\frac{\partial S}{\partial \tau}\frac{\partial \theta}{\partial R^*}\Big|_{0<R^*<S}$$

$$(\text{B.7})\quad St\frac{\partial \theta}{\partial R^*}=\frac{\partial R^*}{\partial \tau}\Big|_{R^*=S}$$

$$(\text{B.8})\quad \frac{\partial \theta}{\partial R^*}=Bi\,\theta\,|_{R^*=0}$$

$$(\text{B.9})\quad \theta=1\,|_{S<R^*<1}$$

$$(\text{B.10})\quad \theta(r,0)=1$$

We solve Eqs. (B.6)–(B.10) numerically and use a finite difference approximation and moving grid approach. We adopt the stability condition used by Ismail and Henriquez (2000)

$$(\text{B.11})\quad \frac{\tau_N}{2R_N^*}\leq \frac{1}{2},$$

where N is the number of points in the grid. We let $n = 0$ at $R^* = 0$ and $n = N$ at $R^* = S$, where S is the position of the condensation front. We use a grid with = 25 grid points as did Ismail and Henriquez (2000).

We test our model by comparing our solution (without advection) to an analytical solution by Pedroso and Domoto (1973). We also write out and solve a similar set of equations for a planar geometry and compare those solutions to our data as well. While our model includes cooling effects from fluid flow, we do not explicitly include the effects of heat transfer among multiple phases and we assume that steam in the clast interior is at the boiling temperature. We use values derived in Section 4.4 to estimate H.

Appendix C. Effective Stefan number

The Stefan number, St, is an important parameter in the Stefan problem and expresses the ratio of sensible to latent heat in a clast. Clasts with lower Stefan number (more latent heat) will take longer to cool and saturate. The Stefan number is traditionally defined as

$$(\text{C.1})\quad St=\frac{(T_f-T_\infty)c_p}{L},$$

where c_p is the solid phase heat capacity and L is the latent heat of vaporization.

Defining a Stefan number in a high porosity clast that contains multiple phases (glass, steam, liquid water, air) is complicated, however, because of the volume changes associated with phase changes and because more thermal mass can be in the rock rather than the vapor. Therefore we make several assumptions and approximations to estimate Stefan numbers for hot and porous pumice.

First, we use an effective heat capacity for the liquid-filled area between the condensation interface and clast exterior, $c_{peff} = (1 - \phi)c_{pr} + \phi c_{pl}$, where c_{pr} is the heat capacity of the glass phase and c_{pl} is the heat capacity of the liquid phase (Fig. 6).

Second, we compare the thermal energy of the rock to the vapor phase. The thermal energy of water vapor at temperature, T, per unit volume is

$$(C.2) \quad H_s = \phi T c_{ps} \rho_s + \phi L \rho_s$$

where c_{ps} is the heat capacity of steam, ρ_s is steam density, L is latent heat. The thermal energy of the glass matrix per unit volume is

$$(C.3) \quad H_g = (1 - \phi) T c_{pr} \rho_r.$$

Using $\rho_s = 1$ kg m^{-3} and $\phi = 0.7$ we find that $\frac{H_s}{H_g} = 10^{-2}$ for $T = 100°C$ and $\frac{H_s}{H_g} = 3 \times 10^{-3}$ for $T = 500°C$. Because $\frac{H_s}{H_g}$ is small, we conclude that much more thermal energy is held within the glass matrix than the vapor phase in steam-filled pumice.

Steam condensation in clast interiors may therefore be limited, not just by the latent heat of condensation, but by the sensible heat of the glass. That is, as a condensation interface moves inward some distance, the heat removed is not only the latent heat of the water vapor, but also the sensible heat of the vapor and glass. We therefore write an effective latent heat that includes the thermal energy of the glass matrix (we neglect the relatively small contribution from vapor sensible heat)

$$(C.4) \quad L_{eff} = \underbrace{\frac{\phi \rho_s (1 - g_f) L}{(1 - \phi)\rho_r + \phi \rho_l}}_{vapor\ latent\ heat} + \underbrace{\frac{(1 - \phi)\rho_r c_{pr}(T - T_f)}{(1 - \phi)\rho_r + \phi \rho_l}}_{glass\ sensible\ heat},$$

where T is clast temperature, T_f is the phase change temperature, and g_f is the fraction of trapped non-condensable gas (e.g., CO$_2$ or air) in the pore space. We normalize clast latent and sensible heat by the density of the liquid saturated rock in Eq. (C.4).

We use Eq. (C.4) to estimate an effective Stefan number for porous clasts that contain water vapor

$$(C.5) \quad St_{eff} = \frac{(T_f - T_\infty)c_{peff}}{L_{eff}}.$$

Using $T = 523°C$, $T_f = 100°C$, $T_\infty = 20°C$, $c_{peff} = 3.2$ kJ kg^{-1} K^{-1}, $c_{pr} = 0.8$ kJ kg^{-1} K^{-1}, $c_{pl} = 4.2$ kJ kg^{-1} K^{-1}, $L = 2200$ kJ kg^{-1}, $\phi = 0.7$, $\rho_s = 1$ kg m^{-3}, $\rho_r = 2400$ kg m^{-3}, $\rho_l = 1000$ kg m^{-3}, and $g_f = 0.2$ we find $St_{eff} = 3.5$. Eqs. (C.4) and (C.5) demonstrate how, as clast initial temperature increases, the effective Stefan number decreases.

Appendix D. Conductive cooling on a sphere

Consider a radially symmetric sphere that cools by conduction and convective heat transferat its outer edge. To determine the temperature distribution $T(r,t)$ inside a sphere we write the 1-D heat equation in spherical coordinates and specify initial and boundary conditions:

$$(D.1) \quad \frac{\partial T}{\partial t} = D_{eff} \left(\frac{2}{r} \frac{\partial T}{\partial r} + \frac{\partial^2 T}{\partial r^2} \right) \bigg| 0 < r < r_o$$

$$(D.2) \quad \frac{\partial T}{\partial r} = 0 \big| r = 0$$

$$(D.3) \quad -k_{eff} \frac{\partial T}{\partial r} = H(T - T_\infty) \big| r = r_o$$

$$(D.4) \quad T(r,0) = T_i$$

where T_∞ is background temperature, T_i is initial temperature, t is time, r is radial position, r_o is sphere radius, k_{eff} is effective thermal conductivity, D_{eff} is effective thermal diffusivity, and H is the heat transfer coefficient. The governing equations can be non-dimensionalized by defining $R = \frac{r}{r_o}$ to be dimensionless radius, $\tau = \frac{D_{eff} t}{r_o^2}$ to be dimensionless time, $\theta(r,t) = \frac{(T(r,t) - T_\infty)}{(T_i - T_\infty)}$ to be dimensionless temperature, and by recalling that $Bi = \frac{H r_o}{k_{eff}}$,

$$(D.5) \quad \frac{\partial \theta}{\partial \tau} = \frac{1}{R} \frac{\partial}{\partial R} \left(R \frac{\partial \theta}{\partial R} \right) \bigg| 0 < R < 1$$

$$(D.6) \quad \frac{\partial \theta}{\partial R} = 0 \big| R = 0$$

$$(D.7) \quad \frac{\partial \theta}{\partial R} + Bi\theta = 0 \big| R = 1$$

$$(D.8) \quad \theta(R,0) = 0.$$

The exact solution to Eqs. (D.5)–(D.8) is given by Eq. (12) and an approximate solution is given by Eq. (13). In Section 4.4 we compare measurements of clast internal temperature to solutions to Eqs. (D.5)–(D.8) to determine stage 2 heat transfer coefficients.

Appendix E. Derivation of equation for trapped gas content

Here we derive an equation that relates change in mass with temperature to changes in fluid fractions within a clast. We can write the total mass of a partially saturated pumice as,

$$(E.1) \quad M_T = M_D + \rho_g V_g + \rho_l V_l,$$

where M_D is the mass of the rock phase (pumice dry mass), ρ_g is the gas density, V_g is the gas volume in the pumice, ρ_l is the liquid density, V_l is the liquid volume with the pumice clast. Because pumice internal volume is conserved, $V_T \phi = V_l + V_g$, where V_T is the total pumice volume and ϕ is porosity. If the mass of non-condensable gas within a pumice doesn't change during stage 2 due to gas trapping and by writing $V_l = (V_T \phi - V_g)$ then the derivative of Eq. (E.1) with respect to temperature is

$$(E.2) \quad \frac{dM_T}{dT} = \frac{d(\rho_l(V_T \phi - V_g))}{dT}.$$

The definition of thermal expansion coefficients (Eq. (14)) can be combined with Eq. (E.2) such that

$$(E.3) \quad \frac{dM_T}{dT} = (V_T\phi - V_g)(-\rho_l \alpha_l) + \rho_l(-\alpha_g V_g).$$

Eq. (E.3) can be further simplified by letting $g_f = \frac{V_g\phi}{V_T}$ be the fraction of trapped gas within the pore space such that

$$(E.4) \quad \frac{dM_T}{dT_r} = -V_T\phi\rho_l\alpha_l - g_f\alpha_l + g_f\alpha_g,$$

where T_r is the temperature at any radial position. We can estimate $\frac{dM_T}{dT}$ by fitting a linear slope to plots of temperature versus submerged weight and then use Eq. (E.4) to estimate trapped gas fraction (Fig. 9). We can use temperature from any radial position, T_r, because in a conductively cooling body the time dependence of internal temperature at any radial position is the same as that at the center point (Incropera et al., 2002).

References

Allen et al., 2008

S. Allen, R. Fiske, Cashman K.**Quenching of steam-charged pumice: implications for submarine pyroclastic volcanism**

Earth Planet. Sci. Lett., 274 (2008), pp. 40-49, 10.1016/j.epsl.2008.06.050

Allen and McPhie, 2000

S. Allen, McPhie J.**Water-settling and resedimentation of submarine rhyolitic pumice at Yali, Eastern Aegean, Greece**

J. Volcanol. Geotherm. Res., 95 (2000), pp. 285-307, 10.1016/S0377-0273(99)00127-4

Allen and McPhie, 2009

S.R. Allen, McPhie J.**Products of Neptunian eruptions**

Geology, 37 (7) (2009), pp. 639-642, 10.1130/G30007A.1

Bagdassarov et al., 1994

N. Bagdassarov, D.B. Dingwell, Webb S.L.**Viscoelasticity of crystal-and bubble-bearing rhyolite melts**

Phys. Earth Planet. Inter., 83 (1994), pp. 83-99, 10.1016/0031-9201(94)90066-3

Bamberger and Prinz, 1986

M. Bamberger, Prinz B.**Determination of heat transfer coefficients during water cooling of metals**

Mater. Sci. Technol., 2 (1986), pp. 410-415

Barker et al., 2012

S. Barker, C. Wilson, J. Baker, M.-A. Millet, M. Rotella, I. Wright, Wysoczanski R.**Geochemistry and petrogenesis of silicic magmas in the intra-oceanic Kermadec arc**

J. Petrol., 54 (2012), pp. 351-391

Batchelor, 1970

G. Batchelor**K. 1967 An Introduction to Fluid Dynamics**

(1970)

Benage et al., 2016

M. Benage, J. Dufek, Mothes P.**Quantifying entrainment in pyroclastic density currents from the Tungurahua eruption, Ecuador: integrating field proxies with numerical simulations**

Geophys. Res. Lett., 43 (2016), pp. 6932-6941, 10.1002/2016GL069527

Bredehoeft and Papaopulos, 1965

J. Bredehoeft, Papaopulos I.**Rates of vertical groundwater movement estimated from the earth's thermal profile**

Water Resour. Res., 1 (1965), pp. 325-328

Bryan et al., 2004

S. Bryan, A. Cook, J. Evans, P. Colls, M. Wells, M. Lawrence, J. Jell, A. Greig, Leslie R.**Pumice rafting and faunal dispersion during 2001–2002 in the southwest Pacific: record of a dacitic submarine explosive eruption from Tonga**

Earth Planet. Sci. Lett., 227 (2004), pp. 135-154, 10.1016/j.epsl.2004.08.009

Burgisser et al., 2017

A. Burgisser, L. Chevalier, J.E. Gardner, Castro J.M.**The percolation threshold and permeability evolution of ascending magmas**

Earth Planet. Sci. Lett., 470 (2017), pp. 37-47, 10.1016/j.epsl.2017.04.023

Cahalan and Dufek, 2017

R. Cahalan, Dufek J.**Numerical modeling of pumice clast heat transfer dynamics in subaqueous eruptions**

AGU Chapman Conference on Submarine Volcanism (2017)

Carey et al., 2014a

R. Carey, S. Allen, J. McPhie, R. Fiske, Tani K.**Submarine silicic explosive eruptions: what can submarine pyroclasts tell us?**

AGU Fall Meeting Abstracts (2014)

Carey et al., 2018

R. Carey, S.A. Soule, M. Manga, J.D. White, J. McPhie, R. Wysoczanski, M. Jutzeler, K. Tani, D. Yoerger, D. Fornari, F. Caratori-Tontini, B. Houghton, S. Mitchell, F. Ikegami, C. Conway, A. Murch, K.Fauria, M. Jones, R. Cahalan,

McKenzie W.**The largest deep-ocean silicic volcanic eruption of the past century**

Sci. Adv., 4 (2018), p. e1701121

Carey et al., 2014b

R.J. Carey, R. Wysoczanski, R. Wunderman, Jutzeler M.**Discovery of the largest historic silicic submarine eruption**

EOS Trans. Am. Geophys. Union, 95 (2014), pp. 157-159, 10.1002/2014EO190001

Cas and Giordano, 2014

R.A. Cas, Giordano G.**Submarine volcanism: a review of the constraints, processes and products, and relevance to the Cabo de Gata volcanic succession**

Ital. J. Geosci., 133 (2014), pp. 362-377, 10.3301/IJG.2014.46

Cashman and Fiske, 1991

K.V. Cashman, Fiske R.S.**Fallout of pyroclastic debris from submarine volcanic eruptions**

Science(Washington), 253 (1991), pp. 275-280

Colombier et al., 2017

M. Colombier, F.B. Wadsworth, L. Gurioli, B. Scheu, U. Kueppers, A. Di Muro, DingwellD.B.**The evolution of pore connectivity in volcanic rocks**

Earth Planet. Sci. Lett., 462 (2017), pp. 99-109, 10.1016/j.epsl.2017.01.011

Degruyter et al., 2010

W. Degruyter, O. Bachmann, Burgisser A.**Controls on magma permeability in the volcanic conduit during the climactic phase of the Kos Plateau tuff eruption (Aegean arc)**

Bull. Volcanol., 72 (2010), p. 63

DeVantier, 1992

L. DeVantier, *et al.***Rafting of tropical marine organisms on buoyant Coralla**

Mar. Ecol. Prog. Ser., 86 (1992)

301–301

Dufek and Bergantz, 2007

J. Dufek, Bergantz G.**Suspended load and bed-load transport of particle-laden gravity currents: the role of particle-bed interaction**

Theor. Comput. Fluid Dyn., 21 (2007), pp. 119-145

Dufek et al., 2007

J. Dufek, M. Manga, Staedter M.**Littoral blasts: pumice-water heat transfer and the conditions for steam explosions when pyroclastic flows enter the ocean**

J. Geophys. Res. Solid Earth, 112 (2007), 10.1029/2006JB004910

Fauria et al., 2017

K.E. Fauria, M. Manga, Wei Z.**Trapped bubbles keep pumice afloat and gas diffusion makes pumice sink**

Earth Planet. Sci. Lett., 460 (2017), pp. 50-59, 10.1016/j.epsl.2016.11.055

Fiske et al., 2001

R.S. Fiske, J. Naka, K. Iizasa, M. Yuasa, Klaus A.**Submarine silicic caldera at the front of the Izu-Bonin arc, Japan: voluminous seafloor eruptions of rhyolite pumice**

Geol. Soc. Am. Bull., 113 (2001), pp. 813-824

Giachetti et al., 2015

T. Giachetti, H.M. Gonnermann, J.E. Gardner, T. Shea, Gouldstone A.**Discriminating secondary from magmatic water in rhyolitic matrix-glass of volcanic pyroclasts using thermogravimetric analysis**

Geochim. Cosmochim. Acta, 148 (2015), pp. 457-476

Gonnermann et al., 2018

H.M. Gonnermann, T. Giachett, line Fliedner, C.T. Nguyen, B.F. Houghton, J.A. Crozier, Carey R.J.**Permeability during magma expansion and compaction**

JGR: Solid Earth (2018)

Head and Wilson, 2003

J.W. Head, Wilson L.**Deep submarine pyroclastic eruptions: theory and predicted landforms and deposits**

J. Volcanol. Geotherm. Res., 121 (2003), pp. 155-193, 10.1016/S0377-0273(02)00425-0

Houghton and Wilson, 1989

B. Houghton, Wilson C.**A vesicularity index for pyroclastic deposits**

Bull. Volcanol., 51 (1989), pp. 451-462

Incropera et al., 2002

F.P. Incropera, D.P. Dewitt, T. Bergman, Lavine A.**Fundamentals of Mass and Heat Transfer**

Australia: John Wiley and Sons (2002)

Ismail and Henrıquez, 2000

K. Ismail, Henrıquez J.**Solidification of PCM inside a spherical capsule**

Energy Convers. Manag., 41 (2000), pp. 173-187

Jutzeler et al., 2017

M. Jutzeler, M. Manga, J. White, P. Talling, A. Proussevitch, S. Watt, M. Cassidy, R. Taylor, A. Le Friant, Ishizuka O.**Submarine deposits from pumiceous pyroclastic density currents traveling over water: an outstanding example from offshore Montserrat (iodp 340)**

Geol. Soc. Am. Bull., 129 (2017), pp. 392-414, 10.1130/B31448.1

Jutzeler et al., 2014

M. Jutzeler, R. Marsh, R.J. Carey, J.D. White, P.J. Talling, Karlstrom L.**On the fate of pumice rafts formed during the 2012 Havre submarine eruption**

Nat. Commun., 5 (2014), 10.1038/ncomms4660

Kano et al., 1996

K. Kano, T. Yamamoto, Ono K.**Subaqueous eruption and emplacement of the Shinjima pumice, Shinjima (Moeshima) Island, Kagoshima Bay, SW Japan**

J. Volcanol. Geotherm. Res., 71 (1996), pp. 187-206, 10.1016/0377-0273(95)00077-1

Klug and Cashman, 1996

C. Klug, Cashman K.V.**Permeability development in vesiculating magmas: implications for fragmentation**

Bull. Volcanol., 58 (2) (1996), pp. 87-100

Manga et al., 2018

M. Manga, K.E. Fauria, C. Lin, S.J. Mitchell, M. Jones, C. Conway, W. Degruyter, B.Hosseini, R. Carey, R. Cahalan, B.F. Houghton, J.D. Whie, M. Jutzeler, S.A. Soule, Tani K.**The pumice raft-forming 2012 Havre submarine eruption was effusive**

Earth Planet. Sci. Lett. (2018)

Mitchell et al., 2018

S.J. Mitchell, I.M. McIntosh, B.F. Houghton, R.J. Carey, Shea T.**Dynamics of a powerful deep submarine eruption recorded in h 2 o contents and speciation in rhyolitic glass: the 2012 Havre eruption**

Earth Planet. Sci. Lett., 494 (2018), pp. 135-147

Mueller et al., 2005

S. Mueller, O. Melnik, O. Spieler, B. Scheu, Dingwell D.B.**Permeability and degassing of dome lavas undergoing rapid decompression: an experimental determination**

Bull. Volcanol., 67 (2005), pp. 526-538

Ongaro et al., 2007

T.E. Ongaro, C. Cavazzoni, G. Erbacci, A. Neri, Salvetti M.-V.**A parallel multiphase flow code for the 3d simulation of explosive volcanic eruptions**

Parallel Comput., 33 (2007), pp. 541-560, 10.1016/j.parco.2007.04.003

Pedroso and Domoto, 1973

R. Pedroso, Domoto G.A.**Inward spherical solidification solution by the method of strained coordinates**

Int. J. Heat Mass Transf., 16 (1973), pp. 1037-1043

Riley et al., 1974

D. Riley, F. Smith, Poots G.**The inward solidification of spheres and circular cylinders**

Int. J. Heat Mass Transf., 17 (12) (1974), pp. 1507-1516

Rotella et al., 2015

M.D. Rotella, C.J. Wilson, S.J. Barker, C.I. Schipper, I.C. Wright, Wysoczanski R.J.**Dynamics of deep submarine silicic explosive eruptions in the Kermadec arc, as reflected in pumice vesicularity textures**

J. Volcanol. Geotherm. Res., 301 (2015), pp. 314-332, 10.1016/j.jvolgeores.2015.05.021

Rotella et al., 2013

M.D. Rotella, C.J. Wilson, S.J. Barker, Wright I.C.**Highly vesicular pumice generated by buoyant detachment of magma in subaqueous volcanism**

Nat. Geosci., 6 (2013), pp. 129-132

Rust and Cashman, 2004

A. Rust, Cashman K.V.**Permeability of vesicular silicic magma: inertial and hysteresis effects**

Earth Planet. Sci. Lett., 228 (2004), pp. 93-107, 10.1016/j.epsl.2004.09.025

Saar and Manga, 1999

M.O. Saar, Manga M.**Permeability-porosity relationship in vesicular basalts**

Geophys. Res. Lett., 26 (1999), pp. 111-114, 10.1029/1998GL900256

Schneider, 1955

P.J. Schneider**Conduction Heat Transfer**

Addison-Wesley Pub. Co. (1955)

Stewart and McPhie, 2004

A.L. Stewart, McPhie J.**An upper pliocene coarse pumice breccia generated by a shallow submarine explosive eruption, Milos, Greece**

Bull. Volcanol., 66 (2004), pp. 15-28

Stroberg et al., 2010

T.W. Stroberg, M. Manga, Dufek J.**Heat transfer coefficients of natural volcanic clasts**

J. Volcanol. Geotherm. Res., 194 (2010), pp. 214-219, 10.1016/j.jvolgeores.2010.05.007

Thomas and Sparks, 1992

R. Thomas, Sparks R.**Cooling of tephra during fallout from eruption columns**

Bull. Volcanol., 54 (1992), pp. 542-553

Vella and Huppert, 2007

D. Vella, Huppert H.E.**The waterlogging of floating objects**

J. Fluid Mech., 585 (2007), pp. 245-254

White et al., 2015

J. White, C. Schipper, Kano K.**Submarine Explosive Eruptions**

The Encyclopedia of Volcanoes (second edition): Amsterdam, Elsevier (2015), pp. 553-569

Whitham and Sparks, 1986

A. Whitham, Sparks R.**Pumice**

Bull. Volcanol., 48 (1986), pp. 209-223

Woods, 2010

A.W. Woods**Turbulent plumes in nature**

Annu. Rev. Fluid Mech., 42 (2010), pp. 391-412

Wright et al., 2009

H.M. Wright, K.V. Cashman, E.H. Gottesfeld, Roberts J.J.**Pore structure of volcanic clasts: measurements of permeability and electrical conductivity**

Earth Planet. Sci. Lett., 280 (2009), pp. 93-104, 10.1016/j.epsl.2009.01.023